The Astronomical Journal, 169:301 (25pp), 2025 June https://doi.org/10.3847/1538-3881/adc736

Stellar Populations and Molecular Gas Composition in the Low-metallicity Environment of WLM

Haylee N. Archer[1,2], Deidre A. Hunter[2], Bruce G. Elmegreen[3], Leslie K. Hunt[4], Rosalia O'Brien[1], Elias Brinks[5], Phil Cigan[6], Monica Rubio[7], Rogier A. Windhorst[1], Rolf A. Jansen[1], and Elijah P. Mathews[8,9,10]
[1] School of Earth and Space Exploration, Arizona State University, Tempe, AZ 85287, USA; harcher@lowell.edu
[2] Lowell Observatory, 1400 W Mars Hill Rd, Flagstaff, AZ 86001, USA
[3] Katonah, NY 10536, USA
[4] INAF, Osservatorio Astrofisico di Arcetri, Largo E Fermi 5, 50125 Firenze, Italy
[5] Centre for Astrophysics Research, University of Hertfordshire, College Lane, Hatfield AL10 9AB, UK
[6] United States Naval Observatory, 3450 Massachusetts Ave NW, Washington, DC 20392, USA
[7] Departamento de Astronomía, Universidad de Chile, Casilla 36-D, Santiago, 8320000, Chile
[8] Department of Astronomy & Astrophysics, The Pennsylvania State University, University Park, PA 16802, USA
[9] Institute for Computation & Data Sciences, The Pennsylvania State University, University Park, PA 16802, USA
[10] Institute for Gravitation and the Cosmos, The Pennsylvania State University, University Park, PA 16802, USA
Received 2024 December 20; revised 2025 March 4; accepted 2025 March 24; published 2025 May 9

Abstract

We investigate the stellar populations and molecular gas properties of a star-forming region within the dwarf irregular (dIrr) galaxy Wolf–Lundmark–Mellote (WLM). Low-metallicity dIrrs like WLM offer a valuable window into star formation in environments that are unlike those of larger, metal-rich galaxies such as the Milky Way. In these conditions, carbon monoxide (CO), typically used to trace molecular clouds, is more easily photodissociated by ultraviolet (UV) radiation, leading to a larger fraction of CO-dark molecular gas, where H_2 exists without detectable CO emission, or CO-dark gas in the form of cold H I. Understanding the molecular gas content and the stellar populations in these star-forming regions provides important information about the role of CO-bright and CO-dark gas in forming stars. Using Hubble Space Telescope imaging across five Wide Field Camera 3 UVIS bands and CO observations from the Atacama Large Millimeter Array, we examine stellar populations within and outside CO cores and the photodissociation region. Our findings indicate similar physical characteristics such as age and mass across the different environments. Assuming 2% of molecular gas is converted to stars, we estimate the molecular gas content and determine that CO-dark gas constitutes a large fraction of the molecular reservoir in WLM. These results are consistent with molecular gas estimates using a previous dust-derived CO-to-H_2 conversion factor (α_{CO}) for WLM. These findings highlight the critical role of CO-dark gas in low-metallicity star formation.

Unified Astronomy Thesaurus concepts: Local Group (929); Dwarf irregular galaxies (417); Star formation (1569); Star forming regions (1565); Stellar populations (1622)

Materials only available in the online version of record: machine-readable tables

1. Introduction

The study of star formation in low-metallicity dwarf galaxies provides valuable insights into the star-forming environments of the most numerous galaxy type in the Universe. Wolf–Lundmark–Mellote (WLM) is a Local Group dwarf irregular (dIrr) galaxy located at a distance of approximately 980 kpc (R. Leaman et al. 2012; S. M. Albers et al. 2019; A. J. Lee et al. 2021; M. J. B. Newman et al. 2024). With a total stellar mass of $1.62 \times 10^7 M_\odot$ (H.-X. Zhang et al. 2012) and a metallicity of $12 + \log(O/H) = 7.8$ (13% $Z_\odot$; H. Lee et al. 2005), WLM is characterized by low mass and low metallicity. The galaxy's isolation, with large separations from both the Milky Way and M31, implies a low likelihood of past interactions with these systems (M. Teyssier et al. 2012; S. M. Albers et al. 2019). This combination of low mass, low metallicity, distance, and isolation makes WLM an ideal laboratory for studying star formation in undisturbed dwarf galaxies, providing insight into star-forming processes in a metal-poor environment.

Metallicity plays a critical role in star formation processes, as metals enhance gas cooling and help shield molecular gas from dissociating radiation (e.g., B. T. Draine & A. Li 2007; Y. Fukui & A. Kawamura 2010; V. Wakelam et al. 2017; O. Osman et al. 2020). In low-metallicity environments, like those found in dwarf galaxies, the reduced metal content limits gas cooling efficiency and molecular cloud shielding, which can impact star formation rates, the initial mass function (IMF), and feedback mechanisms from young stars (e.g., B. G. Elmegreen 1989; N. Brosch et al. 1998; D. A. Hunter et al. 1998; A. K. Leroy et al. 2008; M. Chevance et al. 2020a; D. A. Hunter et al. 2024). These conditions may lead to different star formation dynamics, where molecular gas cooling, cloud collapse, and star formation proceed less efficiently compared to metal-rich environments.

One of the main challenges in studying molecular gas in low-metallicity environments is the detection of molecular hydrogen (H_2), the primary fuel for star formation. Unlike in higher-metallicity galaxies, where carbon monoxide (CO) serves as a reliable tracer for H_2, low-metallicity systems exhibit lower CO abundances due to a lack of shielding against photodissociating ultraviolet (UV) radiation (B. G. Elmegreen et al. 1980; B. G. Elmegreen 1989; C. L. Taylor et al. 1998). This results in a large fraction of CO-dark molecular gas, where

H_2 is present without detectable CO emission (M. G. Wolfire et al. 2010). Consequently, accurate assessment of molecular gas content in these environments requires alternative approaches, such as dust-based methods or [C II] emission, to account for the significant CO-dark gas component (Planck Collaboration et al. 2011; J. L. Pineda et al. 2014; D. Cormier et al. 2017; L. K. Hunt et al. 2023).

This CO-dark gas may contribute extensively to the star-forming material, even though it is invisible in traditional CO surveys (S. C. Madden et al. 2020; S. C. Madden 2022). By studying the stellar populations in and around these regions, we can gain insight into how star formation proceeds in areas with varying molecular gas visibility and density. The characteristics of these populations—such as their ages, masses, and spatial distribution—provide valuable clues about the role of CO-bright and CO-dark gas in forming stars and how the local environment influences star formation efficiency in metal-poor galaxies.

Following the discovery of CO(3–2) emission in two star-forming regions of WLM by B. G. Elmegreen et al. (2013) using the Atacama Pathfinder Experiment (APEX) telescope, M. Rubio et al. (2015) conducted pointed CO(1–0) observations of these regions with the Atacama Large Millimeter Array (ALMA). Their work produced the first detailed map of 10 CO cores in WLM, and M. Rubio et al. (2025, in preparation) have since mapped most of the star-forming area of WLM with ALMA CO(2–1) observations and detected an additional 35 cores. Surrounding six of the original 10 detected cores, [C II] observations traced a photodissociation region (PDR) with a width 5 times larger than the cluster of CO cores, suggesting that molecular clouds at lower metallicities contain [C II] that does not correspond to visible CO or H I, and more compact CO cores compared to those observed in the Milky Way (M. Rubio et al. 2015; P. Cigan et al. 2016).

In this work, we focus on the region defined by the PDR—the only area in WLM with [C II] imaging—which contains six of the CO cores identified by M. Rubio et al. (2015). Studies of other low-metallicity dwarf galaxies have shown that most of the molecular gas reservoir is not well traced by CO(1–0) but can instead be tracked using the [C II] 158 μm line (e.g., M. A. Requena-Torres et al. 2016; S. C. Madden et al. 2020; L. Ramambason et al. 2024). This motivated our choice to use the PDR to define the star-forming region. We compare the stellar populations within that region to those in the surrounding environment, which also contains five additional CO cores detected by M. Rubio et al. (2025, in preparation), to understand their relationship to the CO cores and the PDR.

This paper is organized as follows. In Section 2, we describe our data sources and processing techniques. Section 3 presents the results of our photometric analysis, stellar isochrone fitting, and molecular gas assessment, while Section 4 discusses the implications of these findings for understanding star formation and molecular gas in WLM and similar galaxies. Finally, Section 5 provides a summary and conclusions of our study.

2. Data

2.1. HST GO #17068

We obtained near-ultraviolet (NUV) and optical images covering most of the star-forming area of WLM through the Hubble Space Telescope (HST) GO program #17068 (H. N. Archer et al. 2022a). Focusing on the star-forming region constrained by the [C II]-detected PDR, this project acquired Wide Field Camera 3 (WFC3) UVIS F275W, F336W, F438W, F555W, and F625W images of the region for detecting and analyzing the stellar population. The F275W and F336W UV filters were post-flashed with 20 e^- to account for the charge transfer efficiency (CTE) degradation of the UVIS detector, and the CALWFC3 pipeline implements the CTE-correction code of J. Anderson et al. (2021). We include the effective wavelength and exposure times for each filter in Table 1. The HST images were processed to align the exposures, remove cosmic rays, subtract the background, and correct for geometric distortion using the DrizzlePac tasks TweakReg and AstroDrizzle (S. L. Hoffmann et al. 2021). We utilized the standard calibrated _flc files for WFC3/UVIS, and the pixel scales were kept at their default values of 0.″04. Figure 1 shows a multicolor image combining all five WFC3/UVIS filters, with the PDR, surrounding environment, and CO cores overlaid. All HST data can be found in MAST: 10.17909/xyhn-3z68.

Table 1
HST Filter Wavelengths and Exposure Times

HST Filter Name	Effective Wavelength (Å)	Exp. Time (s)
F275W	2709.7	2220
F336W	3354.5	1230
F438W	4326.2	1760
F555W	5308.4	1125
F625W	6242.6	1050

2.1.1. Photometry

Crowded-field photometry was performed individually on all five HST UVIS images using the Image Reduction and Analysis Facility (IRAF; D. Tody 1986) routine DAOPHOT, derived from the P. B. Stetson (1987) version. To determine the completeness limit for star detection in our crowded-field photometry, we conducted a series of artificial star tests on a band-by-band basis using DAOPHOT. First, we took the total number of stars detected in the image and divided them into magnitude bins. For each bin, we generated a set of artificial (or fake) stars with magnitudes corresponding to that bin and random positions distributed across the entire field, excluding the edges. The number of fake stars inserted in each bin was set to 10% of the total stars originally detected in that magnitude range. These fake stars were then added to the image, and we assessed whether DAOPHOT could retrieve them. This process was repeated 200 times for each of the five images, allowing us to build robust statistics on the detection efficiency at different magnitudes for the different filters. From this, we determined the percentages of stars recovered as a function of magnitude for each filter on a band-by-band basis, shown in Figure 2. The scatter in the artificial star tests is for each filter is shown in Figure 3.

To remove background galaxies, we used the DAOPHOT output parameters sharpness, a goodness-of-fit statistic indicating how much broader the object's profile appears compared to the point-spread function, and chi (χ), the ratio of observed pixel-to-pixel deviation from the profile fit to the expected noise based on Poisson and readout noise. M. Annunziatella et al. (2013) found that plotting sharpness and χ against magnitude clearly separates stars and galaxies, with stars having a sharpness below zero and galaxies showing higher χ values at fainter magnitudes. Due to the overlap of stars and

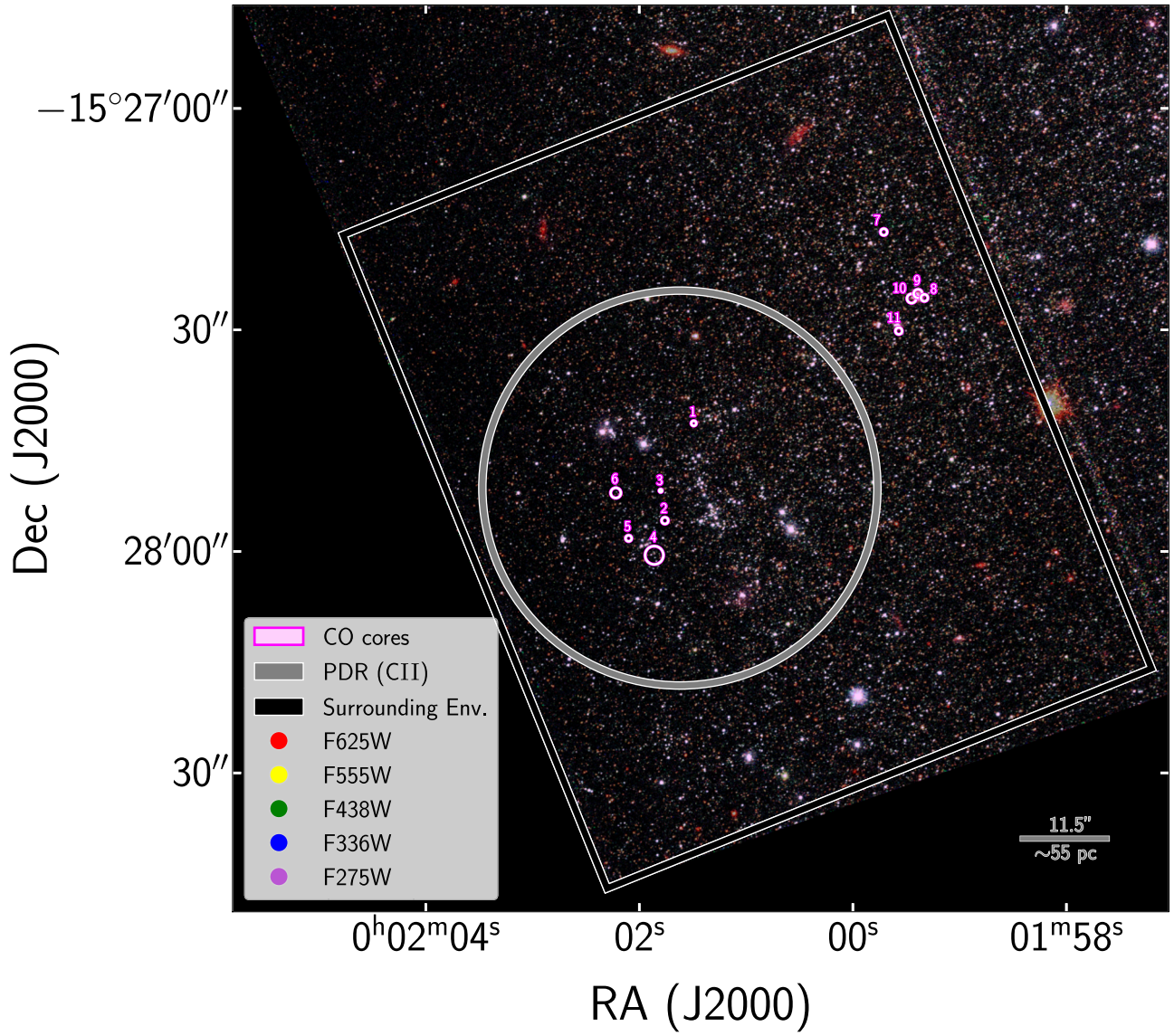

Figure 1. Multicolor image combining the five HST filters, with the outline of the PACS [C II]-detected PDR from P. Cigan et al. (2016, large gray circle) and CO cores (smaller magenta circles) overlaid (M. Rubio et al. 2015). The large black rectangle outlines the environment outside the PDR considered in this work. The legend shows the color assigned to each filter. We also include the 11.″5 (55 pc) PACS beam size, which is the resolution of the PDR, in the bottom-right corner.

galaxies in sharpness and χ at fainter magnitudes, we applied different criteria for sources with Vega magnitudes brighter and fainter than 24. Sources brighter than 24 were classified as stars if their sharpness is less than zero, while sources fainter than 24 were classified as stars if both their sharpness is less than zero and χ is less than 1. Although sharpness and χ were obtained for all five filters, we used F625W values for their clearer population separation. Figure 4 illustrates sharpness and χ values as a function of Vega magnitude for sources detected in the F625W filter. We do not observe a distinct separation between the populations in color and, therefore, do not use color as a criterion for star–galaxy classification. Using single filters to accomplish star–galaxy separation is justified based on a comparison between our Figure 3 and the deeper data of R. A. Windhorst et al. (2011, panels 2–5 in their Figure 10(a)) in WFC3 and ACS filters very similar to ours. Our Figure 3 suggests approximate completeness limits of ∼24–26 mag in F275W to F625W, respectively. To the equivalent depth in the filters from the deeper images of R. A. Windhorst et al. (2011), the large majority of unresolved objects are stars, while almost all galaxies to our shallower depths will be resolved with FWHM $> 0.''1$–$0.''2$. In addition, the stellar density in our WLM fields is far higher than the star counts in the R. A. Windhorst et al. (2011) GOODS-S field at high galactic latitude. The fraction of truly compact galaxies with FWHM $< 0.''2$ to our shallower detection limits is therefore very small. Hence, we do not need to use color for reliable star–galaxy separation.

We first created individual catalogs of stars detected in each of the five filters. To construct a combined catalog of stars detected across all five filters, we performed step-by-step matching, beginning with the UV filters (F275W and F336W), as these are expected to have the shallowest detection limits. Next, we sequentially matched this initial catalog with detections in the F438W, F555W, and F625W filters, combining results at each step. The matching process was carried out using the KDTREE.QUERY_RADIUS function from the SCIKIT-LEARN Python library. A matching radius of $0.''018$ was adopted, which was determined by measuring the

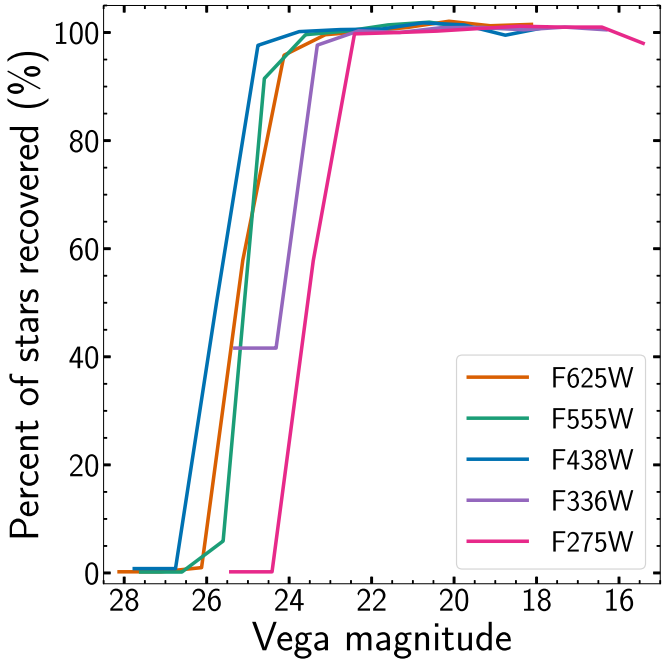

Figure 2. Percent of fake stars recovered using DAOPHOT as a function of Vega magnitude for the F625W (orange), F555W (green), F438W (blue), F336W (purple), and F275W (pink) HST filters.

positional offsets of a small sample of stars identified by eye across multiple filters. The stars in the resulting catalog were examined to ensure there were no spurious detections on diffraction spikes included in the sample. The same methodology was used to create a combined catalog of stars detected across all but the F275W filter.

2.2. Spectral Energy Distribution Fitting

To relate physical stellar properties to observed filter magnitudes and photometric uncertainties, we use the CMD 3.8 tool,[11] which collects the PARSEC 1.2S (A. Bressan et al. 2012; Y. Chen et al. 2014, 2015; J. Tang et al. 2014) and COLIBRI S_37 (P. Marigo et al. 2017; G. Pastorelli et al. 2019, 2020) stellar evolutionary tracks onto a mass–age grid, fixing stellar metallicity to $Z_{\rm ini} = 0.0026$. For each mass–age grid point, CMD provides model fluxes for each of the HST filters used in this work. To generate model fluxes between grid points, we interpolate the model fluxes linearly in $M_{\rm ini}$ and $\log_{10} t$, allowing flux to be generated for any arbitrary mass or age within the range given by CMD. For stellar masses above the maximum mass present in the grid for a given stellar age, we set the flux to $M_{\rm Vega} = 999.99$ as we do not model stellar remnants. Finally, we apply dust attenuation using an SMC extinction curve (K. D. Gordon et al. 2003) in addition to luminosity distance, as follows:

$$m_{\rm predict}(\theta) = m_{\rm interp}(M_{\rm ini}, t) + 5\log_{10} d_L + A_V k_\lambda, \quad (1)$$

where $m_{\rm interp}$ is the flux predicted by the isochrone table interpolation,[12] d_L is the luminosity distance, A_V is the dust attenuation, and k_λ specifies the dust curve and varies by filter:

$$k_\lambda = \begin{cases} 3.625 & \text{F275W}, \\ 1.672 & \text{F336W}, \\ 1.374 & \text{F438W}, \\ 1.000 & \text{F555W}, \\ 0.801 & \text{F625W}. \end{cases} \quad (2)$$

Our four free parameters and their priors are listed in Table 2. For the initial stellar mass, we assume a P. Kroupa (2002) IMF prior, with the prior probability given as

$$\ln p_{\rm M}(M_{\rm ini}) = \begin{cases} (1-\alpha_0)\ln 10 \log_{10} M_{\rm ini} & M_{\rm ini} \leqslant M_1, \\ \Psi_2 + (1-\alpha_1)\ln 10 \log_{10} M_{\rm ini} & M_1 < M_{\rm ini} \leqslant M_2, \\ \Psi_3 + (1-\alpha_2)\ln 10 \log_{10} M_{\rm ini} & M_{\rm ini} > M_2, \end{cases} \quad (3)$$

where $\Psi_2 = (\alpha_1 - \alpha_0)\ln 10 \log_{10} M_1$ and $\Psi_3 = Q_2 + (\alpha_2 - \alpha_1)\ln 10 \log_{10} M_2$, and the α_i and M_i values are adopted from P. Kroupa (2002). Additionally, we assume a uniform prior in stellar age t:

$$\ln p_t(\log_{10} t) = (\ln 10)\log_{10} t, \quad (4)$$

which is equivalent to assuming a constant star formation history (SFH) prior, consistent with the choice made by K. D. Gordon et al. (2016), who also employed Bayesian inference for spectral energy distribution (SED) fitting of stars in M31. It should be noted that neither of these two priors are normalized, since Markov chain Monte Carlo samplers generally only require a probability function that is proportional to the true posterior probability. For the optical dust attenuation A_V, we adopt the normal distribution prior from the Prospector-α physical model (J. Leja et al. 2019). Finally, we adopt a normal distribution prior for the luminosity distance, with a mean of ∼985 kpc and standard deviation of ∼30 kpc to account for the varying distance estimates found in the literature (e.g., R. Leaman et al. 2012; S. M. Albers et al. 2019; A. J. Lee et al. 2021; M. J. B. Newman et al. 2024), and truncated to $\pm 5\sigma$.

Using the flux predicted by the interpolation scheme, we compute the likelihood of the observed fluxes μ_i and their uncertainties σ_i for each filter i given the model θ using a multivariate normal distribution:

$$\ln p(\mu, \sigma|\theta) = -\frac{1}{2}\sum_i \left(\frac{m_{{\rm predict},i}(\theta) - \mu_i}{\sigma_i}\right)^2. \quad (5)$$

Finally, we compute the nonnormalized posterior likelihood as

$$\ln p(\theta|\mu, \sigma) = \ln p(\mu, \sigma|\theta) + \ln p_M(M_{\rm ini}) + \ln p_t(t) + \ln p_d(d_L) + \ln p_{A_V}(A_V). \quad (6)$$

We set the initial position for the sampler at the maximum a posteriori (MAP) location, which is estimated using the Adam optimizer (D. P. Kingma & J. Ba 2017) with $\alpha = 10^{-2}$, run for 10^5 iterations with the Optim.jl Julia package (P. K. Mogensen & A. N. Riseth 2018). Compared to providing a random or zero initial position vector, the MAP location helps the sampler explore the primary mode in the posterior and avoid getting stuck proposing stellar remnant solutions, which may provide a zero gradient since those solutions are fixed at $M_{\rm Vega} = 999.99$ without varying. Once the MAP location is found, we then adapt the step size and mass matrix for the No-U-Turn sampler (NUTS;

[11] Available at http://stev.oapd.inaf.it/cgi-bin/cmd.
[12] All magnitudes given in this work are Vega magnitudes.

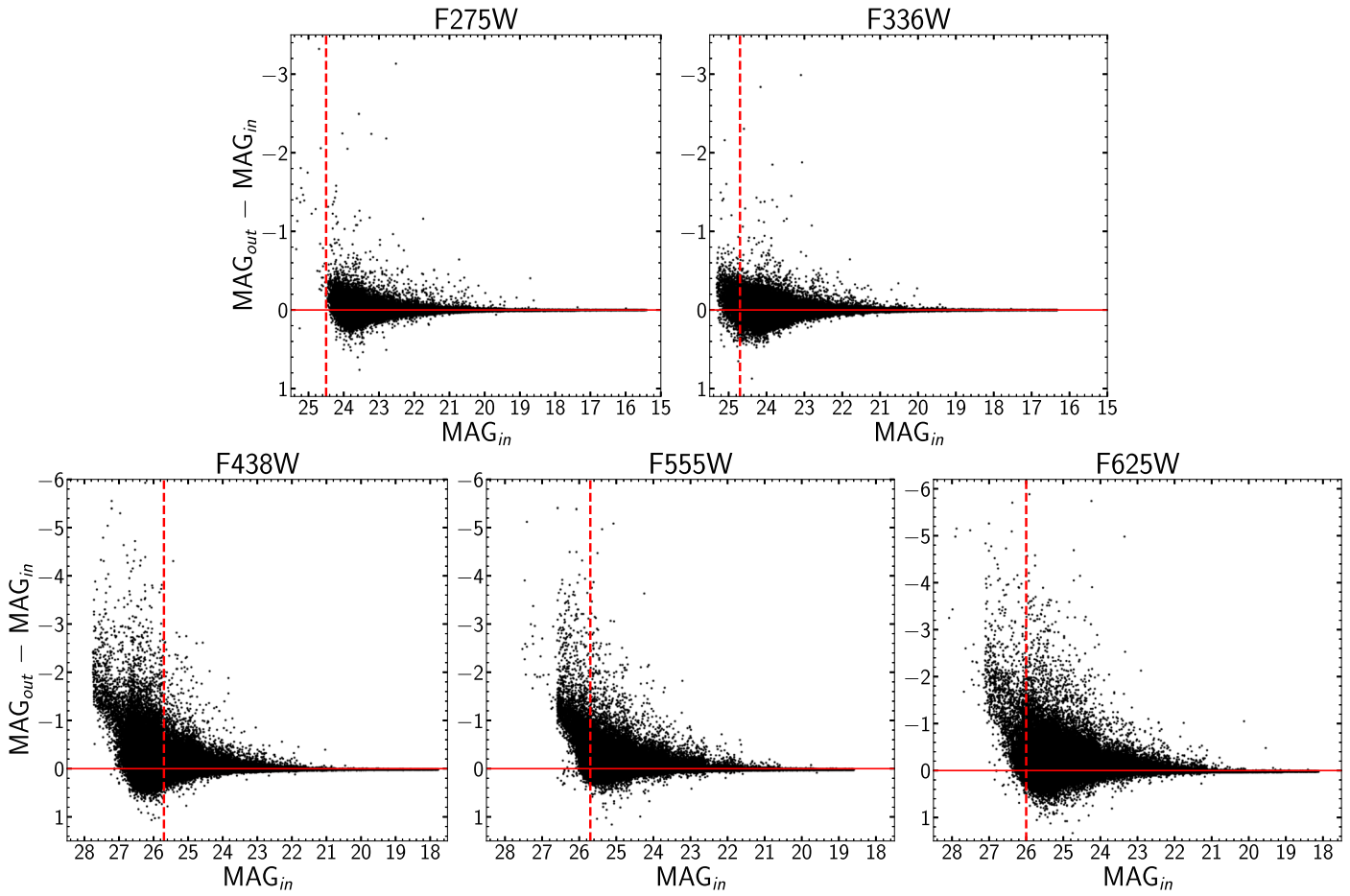

Figure 3. The difference between output and input magnitudes as a function of input magnitude for all artificial stars generated in the artificial star tests for each filter. The solid red horizontal line represents where the input and output magnitudes are identical, while the dashed red vertical line marks the faintest magnitude in that filter observed in the final matched catalog of stars.

M. D. Hoffman & A. Gelman 2011) as implemented in the AdvancedHMC.jl package (K. Xu et al. 2020) using the windowed adaptation scheme from Stan (Stan Development Team 2025), assuming a dense mass matrix and a target acceptance rate of 80%. We run the sampler for 4000 adaptation iterations, after which the mass matrix and step size are frozen. Finally, after adaptation, we use NUTS to draw 4000 samples from the posterior. We estimate each parameter's value as the median (50th percentile) of the parameter's marginalized posterior distribution. The associated uncertainty is quantified as half the difference between the 84th and 16th percentiles: $(P_{84} - P_{16})/2$.

2.3. CO Cores and [C II]

In Cycle 1, M. Rubio et al. (2015) used ALMA to image two star-forming regions in WLM, focusing on CO(1–0) emissions, and detected 10 CO cores. The beam size for these observations was $0\farcs9 \times 1\farcs3$. Of the 10 detected cores, six were located in the PDR, referred to as Region B in B. G. Elmegreen et al. (2013), the WLM-SE region in M. Rubio et al. (2015), and Region 1 in H. N. Archer et al. (2022b), which is the primary focus of this paper. The masses and locations of these six CO cores, labeled as 1 through 6 in Figure 1, can be found in Table 1 of M. Rubio et al. (2015) as regions SE-1 through SE-6. An additional 35 CO cores were detected using CO(2–1) observations at $1''$ resolution (4.8 pc at WLM distance) with ALMA Cycle 6 (M. Rubio et al. 2025, in preparation), all of which were detected outside the PDR as the survey did not include it. Five of these 35 CO cores were included when examining the environment surrounding the PDR to compare stellar populations inside the CO cores and outside the PDR to stellar populations inside the CO cores and inside the PDR. The locations, radii, and virial masses of the 11 CO cores included in this work can be found in Table 3.

The [C II] 158 μm image was obtained using the Photodetector Array Camera and Spectrometer (PACS) spectrometer aboard Herschel for Local Irregulars That Trace Luminosity Extremes, The H i Nearby Galaxy Survey (LITTLE THINGS; P. Cigan et al. 2016). The beam size for the PACS [C II] was $11\farcs5$ (shown in Figure 1), which imaged the targeted region in WLM with a diameter of $54''$, and showed [C II] filling the entire region. We acknowledge that any clouds smaller than $11\farcs5$ would be unresolved in our analysis. Additionally, since the PACS pointing was the only one available for WLM, the [C II] may extend beyond the region defined as the PDR boundary in this study.

3. Results

3.1. Photometry

We separated the stars into four categories based on their coincidence with the PDR and CO cores: (1) stars inside the PDR and projected inside the CO cores, (2) stars inside the

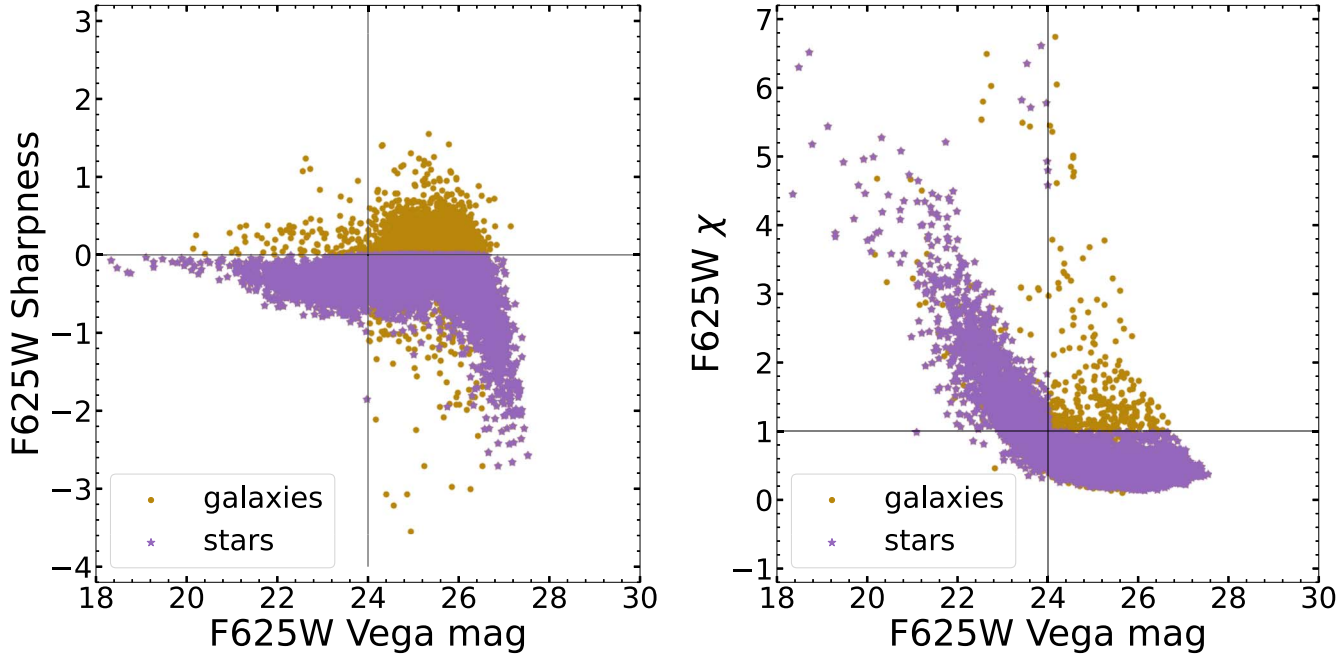

Figure 4. Sharpness (left) and χ (right) values as a function of Vega magnitude for all sources detected in the F625W filter. Gray vertical and horizontal lines are shown to demarcate which sources were stars or galaxies. Sources with a Vega magnitude brighter than 24 were determined to be stars if their sharpness was less than zero (bottom-left quadrant in the sharpness plot), while sources with a Vega magnitude fainter than 24 were determined to be stars if both their sharpness was less than zero and their χ was less than 1 (bottom-right quadrant in both plots). Sources determined to be galaxies are shown as gold points, while sources determined to be stars are shown as purple stars.

Table 2
SED Free Parameters

Parameter	Symbol	Unit	Prior Distribution
Initial mass	$\log_{10}M_{\rm ini}$	$M_\odot$	Kroupa IMF prior (see Equation (3))[a]
Stellar age	$\log_{10}t$	yr	Constant SFH prior (see Equation (4))
Optical dust attenuation	A_V	mag	Normal ($\mu = 0.3$, $\sigma = 1.0$), truncated to the range (0, 4)
Luminosity distance	$\log_{10}d_{\rm L}$	pc	Normal ($\mu = 5.9934$, $\sigma = 0.0132$), truncated to the range (5.9273, 6.0598)

Note.
[a] P. Kroupa (2002).

Table 3
Locations, Radii, and Masses of the CO Cores

CO Core	R.A. (deg)	Decl. (deg)	Radius (pc)	$M_{\rm vir}$ ($M_\odot$)
1[a]	0.5062	−15.462	1.7	1000 ± 700
2[a]	0.5073	−15.466	<1	<400 ± 300
3[a]	0.5075	−15.464	2.2	1100 ± 700
4[a]	0.5078	−15.467	6.0	10,900 ± 3200
5[a]	0.5086	−15.466	2.0	6900 ± 5400
6[a]	0.5092	−15.464	3.4	1400 ± 800
7	0.4988	−15.455	1.9	2100 ± 1300
8	0.4972	−15.457	1.9	900 ± 600
9	0.4975	−15.457	2.5	3900 ± 1300
10	0.4977	−15.457	3.0	1800 ± 1000
11	0.4983	−15.458	1.7	1600 ± 1200

Note.
[a] From Table 1 of M. Rubio et al. (2015).

PDR and outside the CO cores, (3) stars outside the PDR and projected inside the CO cores, and (4) stars outside the the PDR and outside the CO cores. Only four stars are spatially coincident with the CO cores. To better constrain the SED, we include only stars detected in all five filters and in all but the F275W filter. Consequently, there may be stars within the CO that are excluded, as these stars would be embedded and not appear in the bluest filters. This limitation reduces the number of stars available for analysis in these regions. Additionally, some stars coincident with the CO cores may be located in front of the CO rather than within the cores themselves. Stars visible in the reddest HST filter (F625W) but absent from the bluest filters are also detected in the F555W filter, further suggesting that the UVIS data set does not capture embedded stars. Identifying such stars would require the unique high-resolution infrared capabilities of JWST, particularly that of the Mid-Infrared Instrument (MIRI), as the MIRI filters are found to play a crucial role in distinguishing young stellar objects from cool, evolved red stars and background galaxies (J. Peltonen et al. 2024). The JWST Resolved Stellar Populations Early Release Science Program (e.g., D. R. Weisz et al. 2023; M. L. Boyer et al. 2024; K. B. W. McQuinn et al. 2024; M. J. B. Newman et al. 2024) provides publicly available near-infrared photometric catalogs for WLM as part of the JWST Resolved Stellar Populations Early Release Science Program. However, the fields they targeted do not overlap with the region analyzed in this study.

Table 4
R.A., Decl., and Vega Magnitudes for the Five HST Filters for Stars inside the PDR and Projected inside the CO Cores

	R.A. (deg)	Decl. (deg)	F275W (Vega mag)	F336W (Vega mag)	F438W (Vega mag)	F555W (Vega mag)	F625W (Vega mag)
1	0.5077	−15.467	23.07 ± 0.07	23.10 ± 0.05	24.04 ± 0.04	24.04 ± 0.04	23.84 ± 0.06
2	0.5079	−15.467	22.86 ± 0.06	23.23 ± 0.06	24.26 ± 0.04	24.38 ± 0.04	24.30 ± 0.05

Table 5
R.A., Decl., and Vega Magnitudes for the Five HST Filters for Sources inside the PDR and outside the CO Cores

	R.A. (deg)	Decl. (deg)	F275W (Vega mag)	F336W (Vega mag)	F438W (Vega mag)	F555W (Vega mag)	F625W (Vega mag)
1	0.5122	−15.468	23.09 ± 0.08	23.43 ± 0.07	24.03 ± 0.05	23.99 ± 0.05	23.95 ± 0.06
2	0.5131	−15.465	23.66 ± 0.07	23.35 ± 0.06	23.42 ± 0.05	22.68 ± 0.05	21.91 ± 0.05
3	0.5130	−15.464	20.43 ± 0.04	20.86 ± 0.04	22.29 ± 0.05	22.45 ± 0.04	22.25 ± 0.05
4	0.5113	−15.466	20.99 ± 0.04	21.44 ± 0.05	22.89 ± 0.04	23.04 ± 0.05	23.06 ± 0.07
5	0.5109	−15.467	21.70 ± 0.04	22.04 ± 0.05	22.63 ± 0.04	22.71 ± 0.04	22.61 ± 0.06
6	0.5095	−15.471	22.24 ± 0.05	22.65 ± 0.05	23.66 ± 0.04	23.86 ± 0.04	23.74 ± 0.06
7	0.5097	−15.470	22.60 ± 0.05	22.90 ± 0.05	24.08 ± 0.06	24.14 ± 0.05	24.00 ± 0.05
8	0.5121	−15.461	22.93 ± 0.06	22.26 ± 0.05	21.72 ± 0.04	21.55 ± 0.04	21.26 ± 0.06
9	0.5111	−15.463	21.46 ± 0.05	21.35 ± 0.05	21.44 ± 0.06	21.6 ± 0.05	21.32 ± 0.06
10	0.5100	−15.466	22.28 ± 0.05	22.60 ± 0.06	23.82 ± 0.05	24.02 ± 0.05	23.83 ± 0.06

Note. Only a portion of this table is shown here to demonstrate its form and content. A machine-readable version is available for all 443 sources detected inside the PDR and outside the CO cores.

(This table is available in its entirety in machine-readable form in the online article.)

Table 6
R.A., Decl., and Vega Magnitudes for the Five HST Filters for Sources outside the PDR and Projected inside the CO Cores

	R.A. (deg)	Decl. (deg)	F275W (Vega mag)	F336W (Vega mag)	F438W (Vega mag)	F555W (Vega mag)	F625W (Vega mag)
1	0.4975	−15.457	21.51 ± 0.05	21.43 ± 0.04	22.59 ± 0.04	22.31 ± 0.07	22.24 ± 0.04
2	0.4976	−15.457	22.88 ± 0.08	23.38 ± 0.07	24.45 ± 0.07	24.24 ± 0.06	24.13 ± 0.06

Table 7
R.A., Decl., and Vega Magnitudes for the Five HST Filters for Sources outside the PDR and outside the CO Cores

	R.A. (deg)	Decl. (deg)	F275W (Vega mag)	F336W (Vega mag)	F438W (Vega mag)	F555W (Vega mag)	F625W (Vega mag)
1	0.5151	−15.464	22.55 ± 0.05	22.93 ± 0.06	23.95 ± 0.04	24.04 ± 0.04	23.79 ± 0.05
2	0.5124	−15.471	22.68 ± 0.06	22.85 ± 0.05	23.89 ± 0.04	24.05 ± 0.04	23.86 ± 0.09
3	0.5128	−15.470	23.39 ± 0.06	23.29 ± 0.05	24.07 ± 0.05	23.98 ± 0.04	23.92 ± 0.07
4	0.5123	−15.470	23.81 ± 0.09	23.29 ± 0.07	23.57 ± 0.08	23.08 ± 0.06	22.70 ± 0.06
5	0.5123	−15.471	22.74 ± 0.06	22.95 ± 0.06	23.97 ± 0.04	24.00 ± 0.04	23.81 ± 0.05
6	0.5102	−15.476	21.77 ± 0.04	22.07 ± 0.04	23.46 ± 0.05	23.47 ± 0.04	23.22 ± 0.06
7	0.5103	−15.474	24.51 ± 0.18	23.93 ± 0.09	23.69 ± 0.04	23.49 ± 0.04	23.24 ± 0.05
8	0.5095	−15.476	23.87 ± 0.11	23.13 ± 0.07	22.89 ± 0.05	22.61 ± 0.04	22.17 ± 0.06
9	0.5111	−15.471	20.76 ± 0.04	21.13 ± 0.04	22.35 ± 0.04	22.44 ± 0.04	22.53 ± 0.04
10	0.5103	−15.473	22.67 ± 0.05	22.8 ± 0.05	23.36 ± 0.05	23.40 ± 0.04	23.18 ± 0.05

Note. Only a portion of this table is shown here to demonstrate its form and content. A machine-readable version is available for all 566 sources detected outside the PDR and outside the CO cores.

(This table is available in its entirety in machine-readable form in the online article.)

Table 8
R.A., Decl., and Vega Magnitudes for the Four HST Filters for the Star inside the PDR and Projected inside the CO Cores Not Detected in the F275W Filter

	R.A. (deg)	Decl. (deg)	F336W (Vega mag)	F438W (Vega mag)	F555W (Vega mag)	F625W (Vega mag)
1	0.5062	−15.462	24.08 ± 0.10	25.09 ± 0.06	25.35 ± 0.07	24.89 ± 0.08

Table 9
R.A., Decl., and Vega Magnitudes for the Four HST Filters for Sources inside the PDR and outside the CO Cores Not Detected in the F275W Filter

	R.A. (deg)	Decl. (deg)	F336W (Vega mag)	F438W (Vega mag)	F555W (Vega mag)	F625W (Vega mag)
1	0.5128	−15.470	23.18 ± 0.05	23.98 ± 0.05	23.91 ± 0.04	23.86 ± 0.07
2	0.5123	−15.470	23.18 ± 0.07	23.48 ± 0.08	23.01 ± 0.06	22.65 ± 0.06
3	0.5150	−15.462	22.52 ± 0.05	23.49 ± 0.04	23.65 ± 0.04	23.31 ± 0.05
4	0.5111	−15.471	21.01 ± 0.04	22.26 ± 0.04	22.37 ± 0.04	22.47 ± 0.04
5	0.5110	−15.471	19.97 ± 0.07	21.41 ± 0.04	21.50 ± 0.04	21.62 ± 0.06
6	0.5101	−15.472	22.79 ± 0.05	23.81 ± 0.04	23.83 ± 0.04	23.80 ± 0.06
7	0.5134	−15.462	23.90 ± 0.09	23.67 ± 0.04	23.48 ± 0.04	23.22 ± 0.07
8	0.5095	−15.472	23.26 ± 0.07	23.10 ± 0.04	23.05 ± 0.04	22.88 ± 0.05
9	0.5103	−15.466	23.78 ± 0.09	23.61 ± 0.04	23.57 ± 0.04	23.25 ± 0.05
10	0.5113	−15.463	23.89± 0.09	23.36± 0.04	22.47± 0.04	21.95± 0.07

Note. Only a portion of this table is shown here to demonstrate its form and content. A machine-readable version is available for all 144 sources detected inside the PDR and outside the CO cores.

(This table is available in its entirety in machine-readable form in the online article.)

Table 10
R.A., Decl., and Vega Magnitudes for the Four HST Filters for Sources outside the PDR and outside the CO Cores Not Detected in the F275W Filter

	R.A. (deg)	Decl. (deg)	F336W (Vega mag)	F438W (Vega mag)	F555W (Vega mag)	F625W (Vega mag)
1	0.5112	−15.473	24.06 ± 0.09	23.72 ± 0.04	22.90 ± 0.04	22.35 ± 0.06
2	0.5166	−15.456	23.83 ± 0.09	23.71 ± 0.04	23.07 ± 0.04	22.40 ± 0.05
3	0.5094	−15.476	23.70 ± 0.08	22.91 ± 0.05	21.87 ± 0.07	21.12 ± 0.06
4	0.5086	−15.476	23.51 ± 0.08	23.10 ± 0.04	22.27 ± 0.05	21.70 ± 0.07
5	0.5094	−15.474	23.79 ± 0.09	23.67 ± 0.05	23.21 ± 0.04	22.94 ± 0.05
6	0.5132	−15.455	24.33 ± 0.13	24.46 ± 0.06	23.86 ± 0.04	23.24 ± 0.06
7	0.5128	−15.454	23.66 ± 0.07	23.58 ± 0.04	22.91 ± 0.04	22.30 ± 0.04
8	0.5046	−15.477	22.92 ± 0.06	21.17 ± 0.05	19.52 ± 0.04	18.70 ± 0.05
9	0.5107	−15.454	23.79 ± 0.08	23.33 ± 0.04	22.81 ± 0.04	22.08 ± 0.05
10	0.5094	−15.455	24.08± 0.08	23.12± 0.04	22.01± 0.04	21.24± 0.05

Note. Only a portion of this table is shown here to demonstrate its form and content. A machine-readable version is available for all 78 sources detected outside the PDR and outside the CO cores.

(This table is available in its entirety in machine-readable form in the online article.)

Because of the requirement of a detection in the F275W/F336W filters, a larger number of stars detected in the reddest filter, F625W, were excluded. After separating stars from galaxies using the sharpness and χ parameters, the total number of stars detected in F625W was 11,732, while the total number of detected stars in the F275W filter was 1946. The resulting catalog after matching all five filters contains 1013 stars, or around 10% of the stars found in F625W, while the resulting catalog after matching all but the F275W filter includes an additional 223 stars more than the full five-filter catalog.

The R.A., decl., and apparent Vega magnitudes corresponding to the five HST filters for stars in each of the four categories are included in Tables 4, 5, 6, and 7, with the full Tables 5 and 7 available in machine-readable format in the online materials. For stars not detected in the F275W filter, the R.A., decl., and apparent Vega magnitudes corresponding to the other four HST filters are included in Table 8 for stars inside the PDR and projected inside the CO cores, Table 9 for stars inside the PDR and outside the CO cores, and Table 10 for stars outside the PDR and outside the CO cores. The full Tables 9 and 10 are available in machine-readable format in the online materials. No additional stars outside the PDR and projected inside the CO cores were detected after excluding the F275W filter. The sharpness and χ values for all detected filters of the sources determined to be stars are included in Appendix A. We find that all stars, irrespective of proximity to the PDR or CO cores, occupy the same color and magnitude ranges, which can be seen in the F555W versus F555W–F625W and F275W versus F275W–F336W color–magnitude diagrams (CMDs) in Figure 5, and the F336W–F438W versus F438W–F555W color–color diagrams in Figure 6. The scatter in color observed in the CMDs appears to be primarily due to color uncertainties. However, we also find that stars not detected in the F275W filter tend to appear redder in the F555W versus F555W–F625W CMDs, as expected. The redward shift of fainter objects in the F275W versus F275W–F336W CMD may be attributed to reddening or to under-corrected faint-object fluxes resulting from the J. Anderson et al. (2021) CTE correction applied in the pipeline, as demonstrated by R. A. Windhorst et al. (2022). The positions of stars on the color–color diagram in Figure 6 are also consistent with the $U-B$ versus $B-V$ color indices of main-sequence stars (B. Nicolet 1980; A. Bressan et al. 2012; J. Choi et al. 2016). Additionally, stars not detected in the F275W filter are more frequently found in the redder region of the color–color diagrams in Figure 6, aligning with the expected location of cooler main-sequence stars.

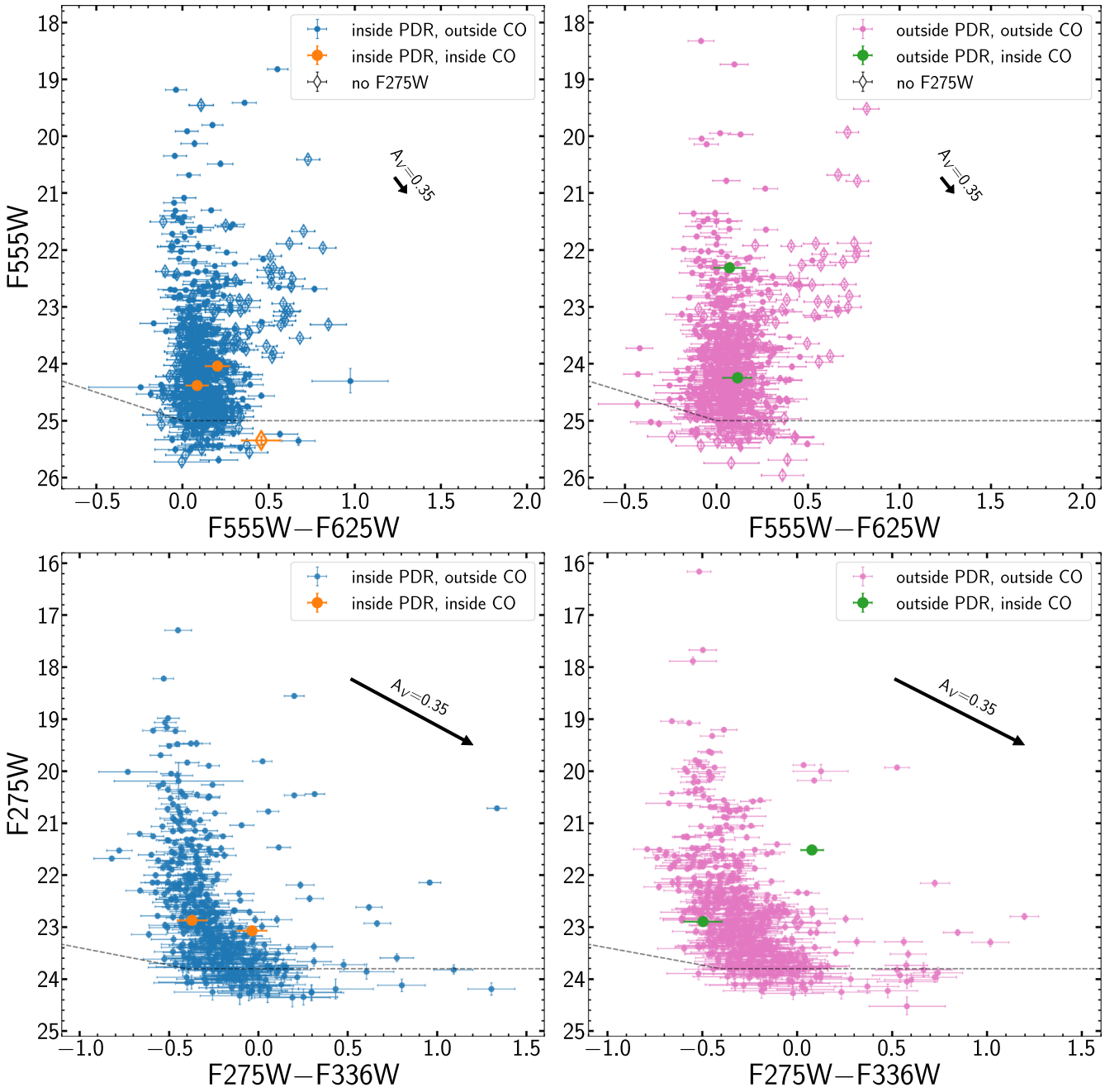

Figure 5. Top left: F555W vs. F555W–F625W color–magnitude diagram (CMD) for stars inside the PDR and outside the CO cores (blue) and stars inside the PDR and projected inside the CO cores (orange). Top right: F555W vs. F555W–F625W CMD for stars outside the PDR and outside the CO cores (pink) and stars outside the PDR and projected inside the CO cores (green). Bottom left: F275W vs. F275W–F6336W CMD for stars inside the PDR and outside the CO cores (blue) and stars inside the PDR and projected inside the CO cores (orange). Bottom right: F275W vs. F275W–F336W CMD for stars outside the PDR and outside the CO cores (pink) and stars outside the PDR and projected inside the CO cores (green). Stars detected in all filters are represented by circles (○), while stars that were not detected in the F275W filter are represented by diamonds (◇). The black arrow in each plot shows the reddening vector for $A_V = 0.35$, the mean A_V of stars in WLM measured by Y. Wang et al. (2022), assuming SMC-like extinction. The error bars in the upper-left corner of each plot demonstrate the mean uncertainty associated with the data shown. The gray dashed line shows the 5σ point-source detection limit for the given filters and exposure times (R. A. Windhorst et al. 2022).

3.2. Masses, Ages, and A_V

Tables 11, 12, 13, 14, 15, 16, and 17 contain the masses, ages, and A_V found using PARSEC for stars in each of the four categories, along with stars not detected in the F275W filter, with the full Tables 12, 14, 16, and 17 included as machine-readable tables in the online materials. The small uncertainties in the inferred physical properties may result from the SED-fitting process rather than reflecting genuinely low uncertainties. We include a corner plot illustrating the SED fit for a representative star from each category in Appendix B. Figure 7 shows histograms of the masses, ages, and A_V of the stars, where we find that stars across all four categories exhibit similar mass, age, and A_V distributions. The mean A_V of all the stars detected is $\sim$0.34 $\pm$ 0.06 mag, which is similar to the mean A_V of stars in WLM measured by Y. Wang et al. (2022), found to be 0.35 mag. This mean extinction value is similar across the different categories. Stellar ages typically range from $\sim$1 to 100 Myr, with older stars likely belonging to the

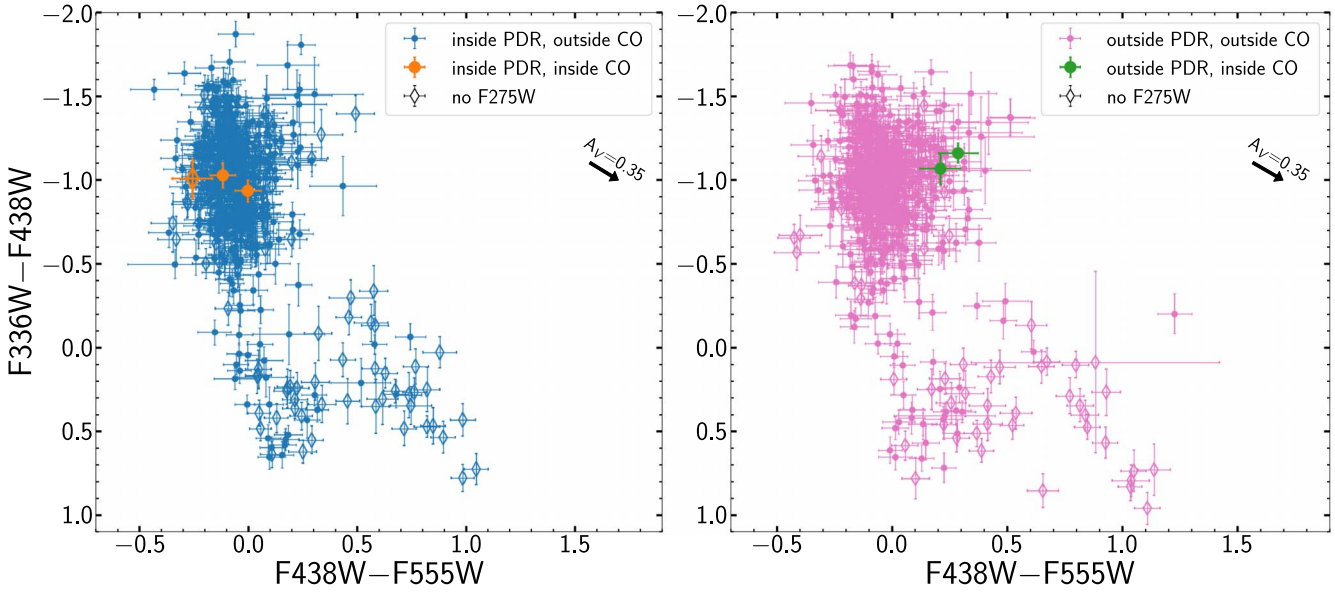

Figure 6. Left: F336W–F438W vs. F438W–F555W color–color diagram for stars inside the PDR and outside the CO cores (blue) and stars inside the PDR and projected inside the CO cores (orange). Right: F336W–F438W vs. F438W–F555W color–color diagram for stars outside the PDR and outside the CO cores (pink), and stars outside the PDR and projected inside the CO cores (green). Stars detected in all filters are represented by circles (○), while stars that were not detected in the F275W filter are represented by diamonds (◇). The black arrow in each plot shows the reddening vector for $A_V = 0.35$, the mean A_V of stars in WLM measured by Y. Wang et al. (2022), assuming SMC-like extinction. The error bars in the upper-left corner of each plot demonstrate the mean uncertainty associated with the data shown.

Table 11
Mass and Age for Stars inside the PDR and Projected inside CO Cores

	$\log_{10}(M/M_\odot)$	$\log_{10}$(age/yr)	A_V/mag
1	0.62 ± 0.03	8.07 ± 0.07	0.20 ± 0.06
2	0.63 ± 0.03	7.96 ± 0.11	0.05 ± 0.04

Table 12
Mass and Age for Stars inside the PDR and outside CO Cores

	$\log_{10}(M/M_\odot)$	$\log_{10}$(age/yr)	A_V/mag
1	0.56 ± 0.01	8.24 ± 0.03	0.09 ± 0.05
2	0.90 ± 0.01	7.56 ± 0.01	0.69 ± 0.02
3	0.95 ± 0.04	7.40 ± 0.10	0.09 ± 0.04
4	0.95 ± 0.05	7.12 ± 0.34	0.07 ± 0.03
5	0.88 ± 0.01	7.55 ± 0.01	0.18 ± 0.04
6	0.67 ± 0.02	7.93 ± 0.06	0.03 ± 0.03
7	0.68 ± 0.04	7.85 ± 0.13	0.10 ± 0.05
8	1.00 ± 0.01	7.37 ± 0.01	0.17 ± 0.03
9	1.13 ± 0.01	7.16 ± 0.01	0.41 ± 0.04
10	0.75 ± 0.05	7.62 ± 0.22	0.10 ± 0.05

Note. Only a portion of this table is shown here to demonstrate its form and content. A machine-readable version is available for all 433 sources detected inside the PDR and outside the CO cores.

(This table is available in its entirety in machine-readable form in the online article.)

Table 13
Mass and Age for Stars outside the PDR and Projected inside CO Cores

	$\log_{10}(M/M_\odot)$	$\log_{10}$(age/yr)	A_V/mag
1	0.97 ± 0.01	7.40 ± 0.01	0.32 ± 0.04
2	0.58 ± 0.02	8.15 ± 0.07	0.04 ± 0.04

Table 14
Mass and Age for Stars outside the PDR and outside CO Cores

	$\log_{10}(M/M_\odot)$	$\log_{10}$(age/yr)	A_V/mag
1	0.64 ± 0.03	8.02 ± 0.07	0.06 ± 0.04
2	0.68 ± 0.03	7.90 ± 0.10	0.13 ± 0.05
3	0.59 ± 0.02	8.18 ± 0.05	0.26 ± 0.04
4	0.97 ± 0.01	7.40 ± 0.01	1.00 ± 0.03
5	0.65 ± 0.03	8.00 ± 0.09	0.14 ± 0.05
6	0.82 ± 0.04	7.56 ± 0.14	0.14 ± 0.04
7	0.91 ± 0.01	7.50 ± 0.01	1.18 ± 0.05
8	0.91 ± 0.01	7.51 ± 0.01	0.61 ± 0.04
9	0.82 ± 0.01	7.69 ± 0.01	0.04 ± 0.02
10	0.78± 0.01	7.75± 0.01	0.26± 0.04

Note. Only a portion of this table is shown here to demonstrate its form and content. A machine-readable version is available for all 566 sources detected outside the PDR and outside the CO cores.

(This table is available in its entirety in machine-readable form in the online article.)

underlying disk population. We note that clusters of closely packed stars may not be fully resolved into individual components.

We also find no correlation is observed between the spatial locations of stars and their respective masses, ages, or A_V as shown in Figure 8. However, we identify some structure and clusters of younger stars near the center of the PDR, which align with regions bright in the far-ultraviolet (FUV). A three-color image of the region is shown in Figure 9, where red corresponds to the HST F336W image, green corresponds to the HST F275W image, and blue corresponds to the FUV image from the NASA Galaxy Evolution Explorer (GALEX) satellite (D. C. Martin et al. 2005; H.-X. Zhang et al. 2012).[13]

[13] GALEX was operated for NASA by the California Institute of Technology under NASA contract NAS5-98034.

Table 15
Mass and Age for the Star inside the PDR and Projected inside CO Cores Not Detected in the F275W Filter

	$\log_{10}(M/M_{\odot})$	$\log_{10}$(age/yr)	A_V/mag
1	0.62 ± 0.06	7.71 ± 0.41	0.34 ± 0.17

Table 16
Mass and Age for Stars inside the PDR and outside CO Cores Not Detected in the F275W Filter

	$\log_{10}(M/M_{\odot})$	$\log_{10}$(age/yr)	A_V/mag
1	0.61 ± 0.01	8.13 ± 0.03	0.33 ± 0.10
2	1.20 ± 0.03	7.09 ± 0.04	2.55 ± 0.09
3	0.79 ± 0.05	7.72 ± 0.11	0.55 ± 0.13
4	0.90 ± 0.04	7.52 ± 0.08	0.14 ± 0.10
5	1.24 ± 0.09	6.87 ± 0.28	0.33 ± 0.10
6	0.72 ± 0.05	7.83 ± 0.14	0.36 ± 0.15
7	1.04 ± 0.01	7.31 ± 0.01	2.11 ± 0.06
8	1.07 ± 0.01	7.26 ± 0.01	1.88 ± 0.05
9	0.95 ± 0.01	7.45 ± 0.01	1.65 ± 0.08
10	0.91 ± 0.01	7.52 ± 0.01	1.15 ± 0.07

Note. Only a portion of this table is shown here to demonstrate its form and content. A machine-readable version is available for all 144 sources detected inside the PDR and outside the CO cores.

(This table is available in its entirety in machine-readable form in the online article.)

The mean velocity dispersion in the region is approximately 8 km s^{-1} (G. Iorio et al. 2017), indicating that stars could have been dispersed by nearly 82 pc over 10 Myr. This dispersion may explain the scattering of young stars observed outside the PDR, which has a radius of ∼130 pc. Additionally, Figure 9 highlights ongoing star formation beyond the PDR, which may not be directly linked to the same star-forming event and could account for the young stars seen outside the PDR.

3.3. Gas Mass

To get a comprehensive view of the gas in our targeted region, we combined our HST and CO data with extant H I masses of the region. The H I mass comes from converting the H I surface density ($\Sigma_{\rm H\,I}$) in Table 2 of H. N. Archer et al. (2022b) to mass. The robust-weighted $\Sigma_{\rm H\,I}$ map was acquired with the Karl G. Jansky Very Large Array (VLA) for LITTLE THINGS, a multiwavelength survey of 37 nearby dIrr galaxies and four nearby blue compact dwarf (BCD) galaxies (D. A. Hunter et al. 2012). We include the mass of the H I atomic gas for this region in Table 18.

To determine the amount of CO-dark molecular gas in the region, we first found the total mass of young stars detected in our region. We estimated the number of detected disk stars in the PDR to be approximately 400. This number also approximately corresponds to the number of stars with ages greater than 30 Myr. Only including stars younger than 30 Myr —the more recent star formation—we estimate the total stellar mass of young stars in our sample to be ∼2000 $M_{\odot}$. The absence of low-mass stars in our sample due to completeness suggests that the total stellar mass is likely much greater than this estimate by a factor of 2 or 3, considering a standard IMF. M. R. Krumholz et al. (2012) find that approximately 1% ± 2% of the molecular gas is converted to stars per local freefall time. For our region, spanning 260 pc in diameter and assuming a velocity dispersion comparable to the stellar dispersion of 8 km s^{-1}, the turbulence crossing time is 32 Myr, which is comparable to the selected age window for our stellar mass. The timescale is also comparable to that of large-scale star formation in the LMC, which is ∼20 Myr on this scale from Figure 1 in B. G. Elmegreen (2000). Taking these timescales as the effective freefall time over the large PDR region considered here, and a conservative estimate of 2% of the gas mass converting to stars in this time, we find the total star-forming gas mass in the PDR using our estimated stellar mass is then

$$2 \times 10^3\, M_{\odot} \,/\, 0.02 \approx 1 \times 10^5\, M_{\odot}. \quad (7)$$

Accounting for the total virial mass of the six CO cores in the region, ∼20,000 $M_{\odot}$, we find the CO-dark molecular gas mass to be

$$1 \times 10^5\, M_{\odot} - 2 \times 10^4\, M_{\odot} = 8 \times 10^4 \quad M_{\odot}, \quad (8)$$

suggesting that approximately 80% of the molecular gas mass is CO-dark. Assuming 1% or 3% of the molecular gas is converted to stars instead yields a CO-dark gas percentage of 90% or 70%, respectively. The total CO virial mass, total stellar mass, total estimated molecular gas mass, and total estimated CO-dark gas mass, along with their associated uncertainties, are included in Table 18.

Table 17
Mass and Age for Stars outside the PDR and outside CO Cores Not Detected in the F275W Filter

	$\log_{10}(M/M_{\odot})$	$\log_{10}$(age/yr)	A_V/mag
1	1.06 ± 0.01	7.30 ± 0.01	2.26 ± 0.03
2	1.29 ± 0.01	6.96 ± 0.01	3.07 ± 0.06
3	1.52 ± 0.01	6.77 ± 0.01	3.89 ± 0.06
4	1.52 ± 0.01	6.76 ± 0.01	3.61 ± 0.06
5	1.13 ± 0.01	7.16 ± 0.01	2.44 ± 0.08
6	1.12 ± 0.05	7.17 ± 0.09	2.70 ± 0.13
7	1.10 ± 0.01	7.21 ± 0.01	2.60 ± 0.09
8	2.02 ± 0.01	6.44 ± 0.01	4.00 ± 0.01
9	1.03 ± 0.01	7.35 ± 0.01	1.93 ± 0.02
10	1.63 ± 0.01	6.66 ± 0.01	3.99 ± 0.01

Note. Only a portion of this table is shown here to demonstrate its form and content. A machine-readable version is available for all 78 sources detected outside the PDR and outside the CO cores.

(This table is available in its entirety in machine-readable form in the online article.)

4. Discussion

Estimating molecular gas mass in low-metallicity galaxies like WLM remains a significant challenge due to the high fraction of CO-dark gas. B. G. Elmegreen et al. (2013) estimated $\alpha_{\rm CO}$ for WLM using dust mass inferred from 160 μm emission from the Spitzer Local Volume Survey (D. A. Dale et al. 2009) and 870 μm emission from the APEX telescope. By adjusting the dust-to-gas ratio for WLM's lower metallicity, they determined a dust-derived $\alpha_{\rm CO}$ of 124 ± 60$M_{\odot}$ pc^{-2} K^{-1} km^{-1} s. Using this $\alpha_{\rm CO}$ value and the CO core

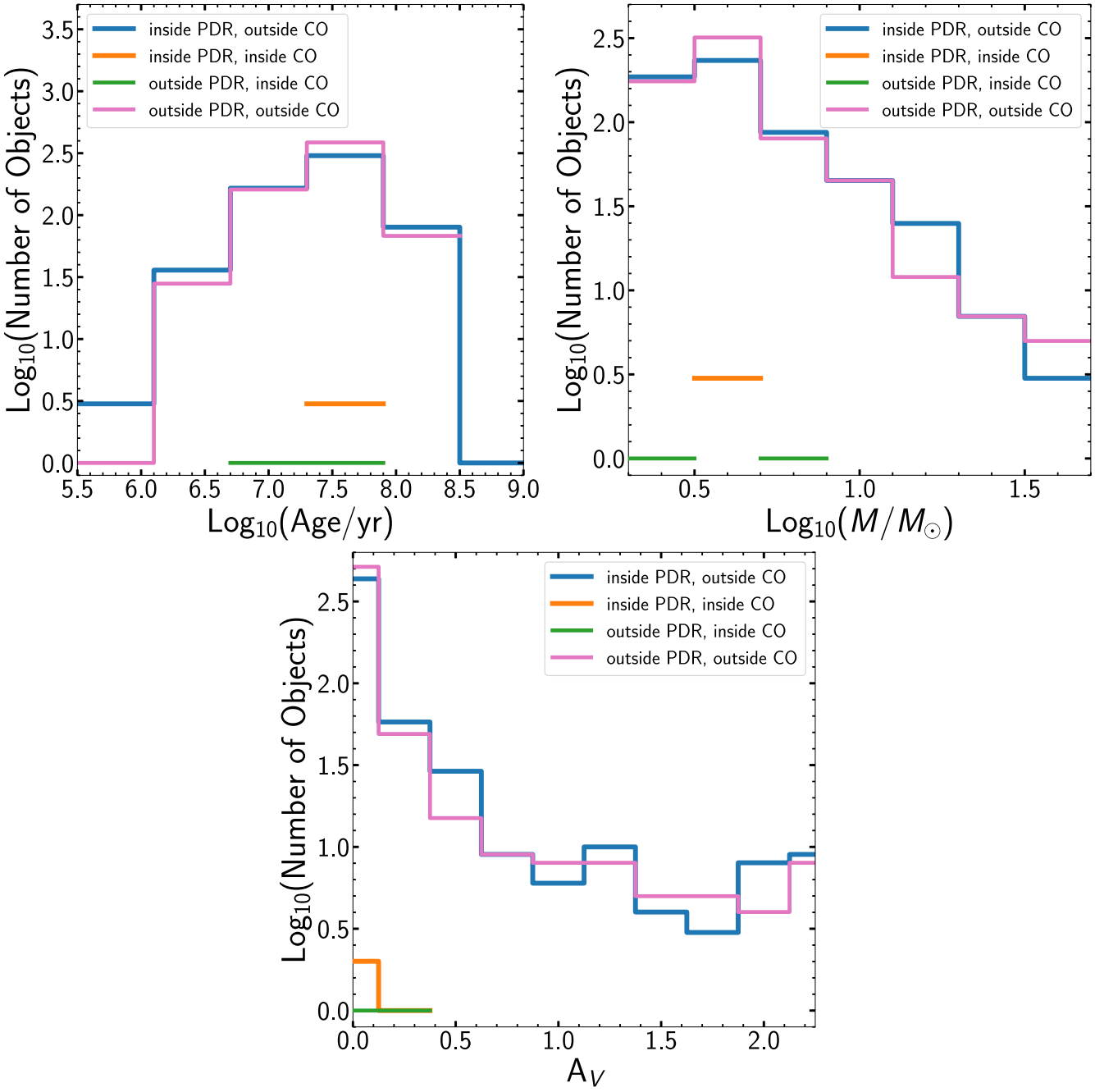

Figure 7. Histograms of the ages (top left), masses (top right), and A_V (bottom) for stars inside the PDR and outside the CO cores (blue), stars inside the PDR and projected inside the CO cores (orange), stars outside the PDR and projected inside the CO cores (green), and stars outside the PDR and outside the CO cores (pink). Clusters of closely packed stars may not be resolved into individual components.

luminosity in our region, the total H_2 mass would be

$$\begin{aligned} M_{\rm gas} &= \alpha_{\rm CO} \times L_{\rm CO} \\ &= (124 \pm 60\, M_\odot\ {\rm pc^{-2}\ K^{-1}\,km^{-1}\ \ s}) \\ &\quad \times (935 \pm 60\ {\rm K\ km\ s^{-1}\,pc^2}) \\ &\approx 115,900 \pm 5,700\, M_\odot, \end{aligned} \tag{9}$$

where $L_{\rm CO}$ is the summed $L_{\rm CO}$ values for the six CO cores in the region from M. Rubio et al. (2015; their Table 1). Alternatively, computing the $\alpha_{\rm CO}$ from our total molecular gas mass of $1 \times 10^5 M_\odot$, we find

$$\begin{aligned} \alpha_{\rm CO} &= M_{\rm gas}/L_{CO} \\ &= \frac{(1 \times 10^5 \pm 5 \times 10^4\, M_\odot)}{(935 \pm 60\ {\rm K\ km\ s^{-1}\,pc^2})} \\ &\approx 100 \pm 50\, M_\odot\ {\rm pc^{-2}\ K^{-1}\,km^{-1}\,s}, \end{aligned} \tag{10}$$

which is consistent with the dust-derived $\alpha_{\rm CO}$ found by B. G. Elmegreen et al. (2013).

The high fraction of CO-dark gas in WLM indicates that a substantial portion of the molecular gas available for star

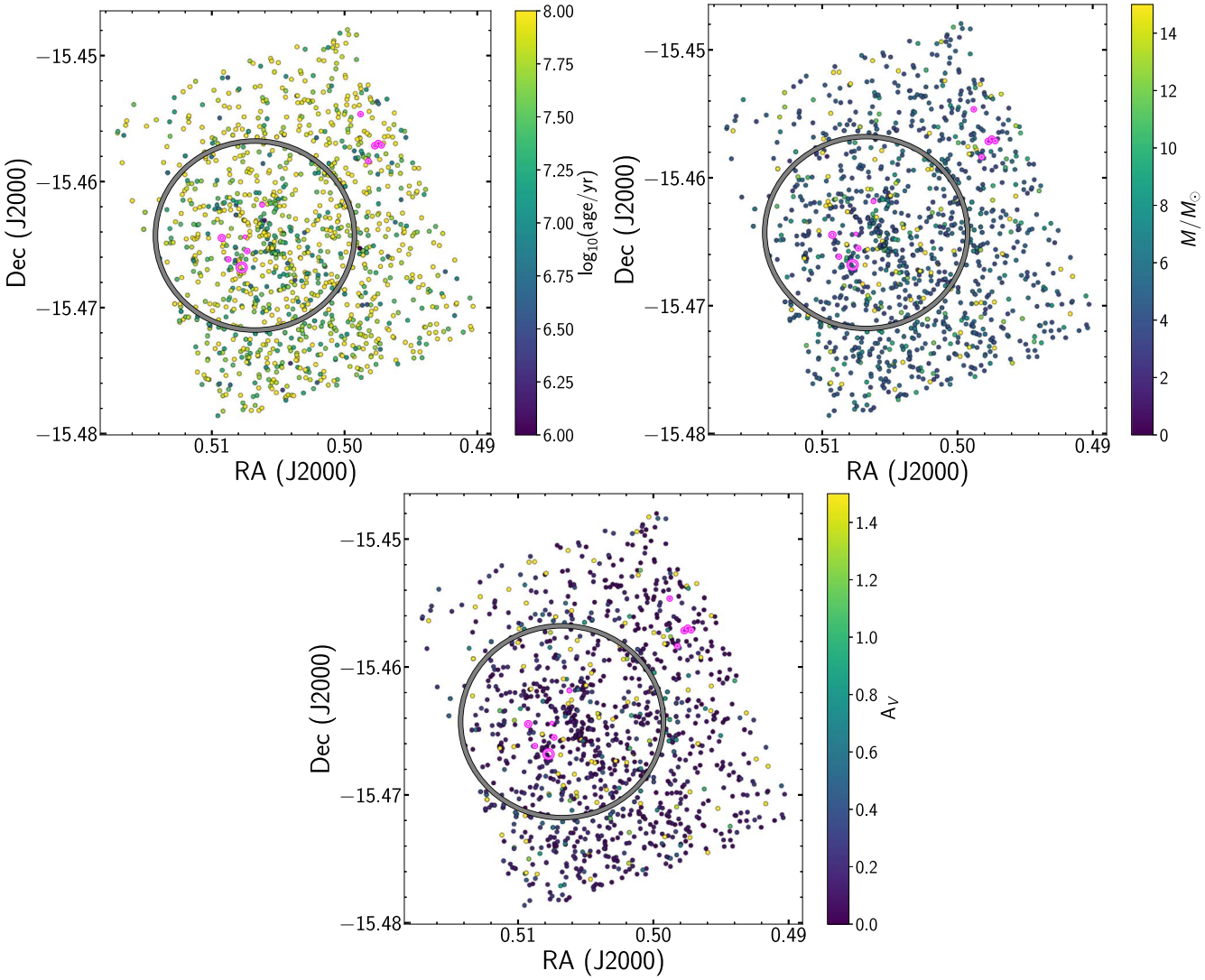

Figure 8. Plots showing the spatial distribution of stars, color-coded by their ages (top left), masses (top right), and A_V (bottom). The large gray circle demarcates the PDR, while the smaller magenta circles show the locations and sizes of the CO cores.

formation exists in a state not directly detectable via CO emission. Studies of other low-metallicity galaxies such as the SMC and LMC and the Dwarf Galaxy Survey find 70%–100% of the molecular hydrogen in low-metallicity galaxies ($Z = 0.02$–$0.6Z_{\odot}$) is CO-dark, increasing with lower metallicity (e.g., M. A. Requena-Torres et al. 2016; M. Chevance et al. 2020b; S. C. Madden et al. 2020; L. Ramambason et al. 2024), which is consistent with our estimated CO-dark gas percentage. Similar to the tiny CO cores detected in WLM, H. P. Saldaño et al. (2023) find that the molecular mass associated with CO clouds in the SMC is primarily concentrated in low-mass clouds distributed throughout the galaxy. This reinforces the understanding that CO-bright regions correspond to the densest, most shielded parts of molecular clouds in low-metallicity environments, while CO-dark regions constitute a diffuse and widespread reservoir of H_2 (M. G. Wolfire et al. 2010; M. R. Krumholz et al. 2012; A. D. Bolatto et al. 2013) or cold H I (C.-Y. Hu et al. 2021, 2022, 2023). These findings underscore the necessity of accounting for CO-dark gas when evaluating the star formation potential of galaxies, particularly in low-metallicity conditions. The agreement between the molecular gas mass inferred from dust measurements (B. G. Elmegreen et al. 2013) and that estimated by combining stellar mass with an assumed 2% star formation efficiency is encouraging. If the dust-related total gas mass is assumed to be the most reliable, then the missing low-mass stars suggest that the product of the efficiency per unit freefall time and the number of freefall times for star formation could be low by a factor of ∼2, which is the likely correction for stellar mass given a standard IMF. For example, the 30 Myr window for our evaluation of young stellar mass could represent two freefall times on this large scale, rather than one as assumed.

5. Summary and Conclusions

In this study, we explored the stellar and gas characteristics within the nearby galaxy WLM using multiwavelength HST imaging and ALMA CO(1–0) and CO(2–1) observations. By employing photometry across five HST filters ranging from 2709.7 to 6242.6 Å, we classified stars and distinguished them from background galaxies, allowing us to analyze stellar masses, ages, and A_V using the PARSEC isochrone models. Our results demonstrate that stars located within the PDR and the CO cores, as well as those outside these regions, exhibit

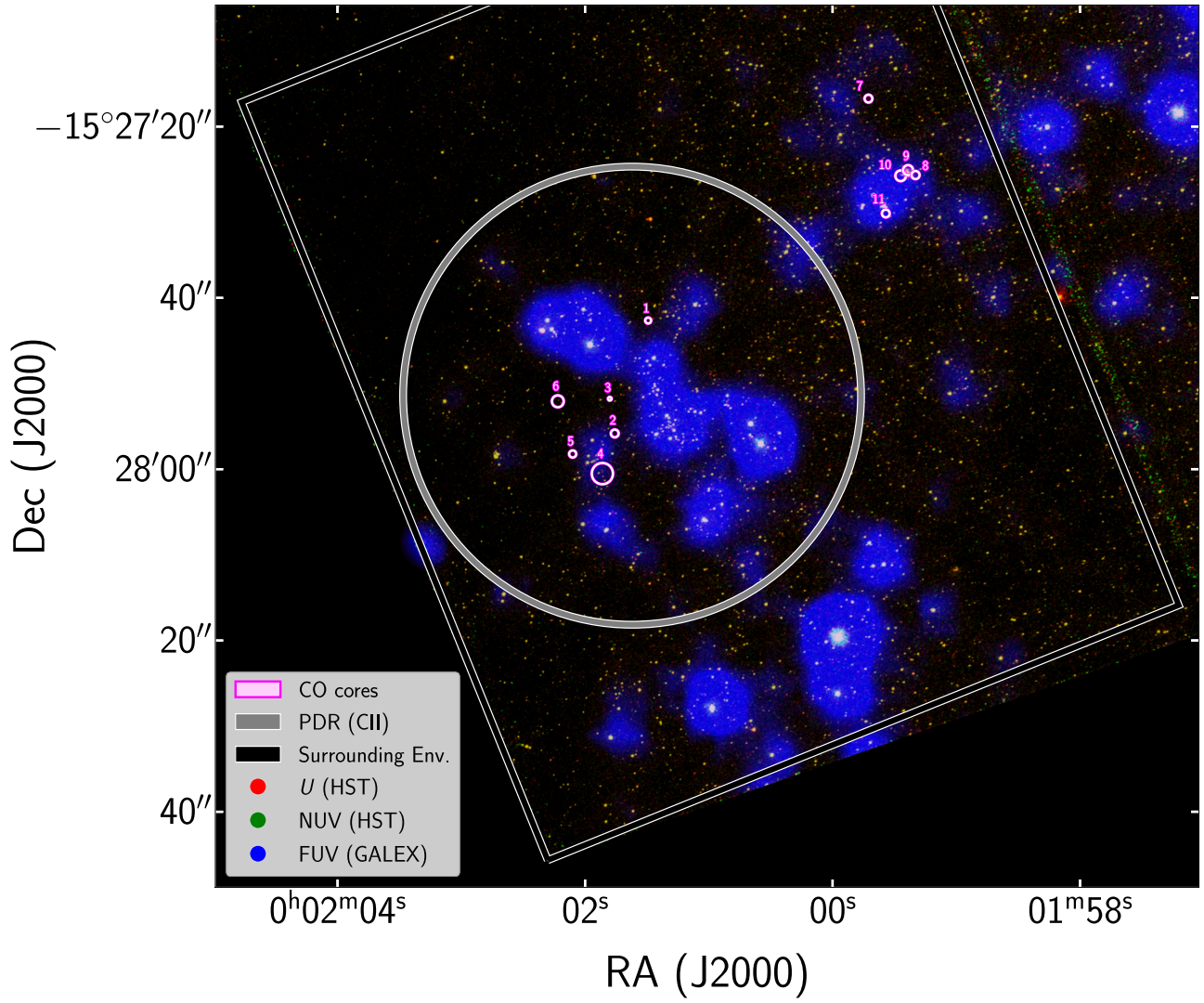

Figure 9. Three-color composite image combining the HST F336W (red), HST F275W (green), and GALEX FUV (blue) images of the region, highlighting how the UV clumps of star formation correspond to the structures and clusters of younger stars within the PDR shown in Figure 8.

Table 18
Gas Masses in the Targeted Region

Type	Mass ($M_\odot$)
H I	1,620,000 ± 600
Stars	2,000 ± 300
CO_{vir}	20,000 ± 6,000
Total (molecular)[a]	100,000 ± 5,000
CO-dark[a]	80,000 ± 5,000

Note.
[a] Assuming 2% ± 1% of molecular gas is converted to stars (M. R. Krumholz et al. 2012).

similar distributions in age, mass, and optical depth, indicating a uniform stellar population across the observed area.

To provide a comprehensive assessment of the gas content, we incorporated existing H I data and estimated the total molecular gas mass, including contributions from CO-dark molecular gas. Our analysis revealed a significant fraction of CO-dark gas, emphasizing its critical role in molecular gas mass estimates that cannot rely solely on CO observations. Additionally, the dust-derived α_{CO} for WLM from B. G. Elmegreen et al. (2013) yields a total molecular gas mass consistent with our estimate based on stellar mass and an assumed star formation efficiency of 2%. However, the stellar mass estimate excludes lower-mass stars that were not detected in our sample. This agreement suggests that combining stellar mass with a 2% star formation efficiency provides an alternative for estimating total molecular gas mass in star-forming regions when dust and CO data are unavailable, though both methods likely underestimate the actual molecular gas mass.

This work examines the molecular gas composition and star formation processes in low-metallicity environments. The results highlight the critical role of CO-dark gas in these systems. Expanding this analysis to a larger sample of star-forming regions within WLM and other low-metallicity galaxies could determine whether the high CO-dark gas content observed in this region is a common characteristic or a unique feature. Such investigations would enhance our understanding of the gas reservoirs that fuel star formation

across diverse galactic environments, and contribute to a more comprehensive framework for star formation in the local Universe.

Acknowledgments

This research is based on observations made with the NASA/ESA Hubble Space Telescope obtained from the Space Telescope Science Institute, which is operated by the Association of Universities for Research in Astronomy, Inc., under NASA contract NAS 5-26555. These observations are associated with program HST-GO-17068.

M.R. wishes to acknowledge support from ANID(CHILE) through Basal FB210003.

This paper makes use of the following ALMA data: ADS/JAO.ALMA#2012.1.00208.S. ALMA is a partnership of ESO (representing its member states), NSF (USA), and NINS (Japan), together with NRC (Canada), MOST and ASIAA (Taiwan), and KASI (Republic of Korea), in cooperation with the Republic of Chile. The Joint ALMA Observatory is operated by ESO, AUI/NRAO and NAOJ. The National Radio Astronomy Observatory is a facility of the National Science Foundation operated under cooperative agreement by Associated Universities, Inc.

We thank the referee for their thorough review and constructive feedback, which significantly improved the quality and clarity of this manuscript.

Lowell Observatory sits at the base of mountains sacred to tribes throughout the region. We honor their past, present, and future generations, who have lived here for millennia and will forever call this place home.

Facilities: ALMA, HST(WFC3/UVIS).

Software: IRAF (D. Tody 1986), scikit-learn (F. Pedregosa et al. 2011), AdvancedHMC.jl (K. Xu et al. 2020), CMD (A. Bressan et al. 2012; Y. Chen et al. 2014, 2015; J. Tang et al. 2014; P. Marigo et al. 2017; G. Pastorelli et al. 2019, 2020), Julia (J. Bezanson et al. 2017), Matplotlib (J. D. Hunter 2007), NumPy (C. R. Harris et al. 2020), Optim.jl (P. K. Mogensen & A. N. Riseth 2018).

Appendix A
Sharpness and Chi Parameters

The sharpness and chi parameters for all objects determined to be stars are included in Tables 19, 20, 21, 22, 23, 24, and 25. The full Tables 20, 22, 24, and 25 are available in machine-readable format in the online materials.

Table 19
The Sharpness and Chi Parameters for the Five HST Filters for Sources inside the PDR and Projected inside the CO Cores

	F275W Sharpness	F275W χ	F336W Sharpness	F336W χ	F438W Sharpness	F438W χ	F555W Sharpness	F555W χ	F625W Sharpness	F625W χ
1	0.12	0.25	−0.07	0.23	−0.06	0.5	−0.06	0.57	−0.43	0.89
2	0.01	0.21	−0.03	0.34	0.01	0.37	0.02	0.38	−0.08	0.54

Table 20
The Sharpness and Chi Parameters for the Five HST Filters for Sources inside the PDR and outside the CO Cores

	F275W Sharpness	F275W χ	F336W Sharpness	F336W χ	F438W Sharpness	F438W χ	F555W Sharpness	F555W χ	F625W Sharpness	F625W χ
1	−0.07	0.33	−0.21	0.35	−0.18	0.70	−0.11	0.82	−0.32	0.85
2	−0.01	0.11	−0.16	0.26	−0.18	0.96	−0.10	1.08	−0.35	2.75
3	−0.09	1.19	0.09	0.86	−0.09	1.14	−0.21	0.89	−0.07	1.92
4	−0.07	0.64	−0.22	0.86	−0.01	0.75	−0.09	1.40	−0.56	1.69
5	−0.16	0.53	−0.34	0.76	−0.22	1.20	−0.12	1.22	−0.37	2.17
6	−0.16	0.44	0.11	0.41	−0.04	0.48	−0.09	0.63	−0.44	1.08
7	−0.16	0.28	−0.11	0.33	−0.33	0.62	−0.30	0.63	−0.21	0.62
8	0.01	0.20	−0.17	0.54	−0.14	1.93	−0.04	2.09	−0.31	3.81
9	0.10	0.77	0.23	1.09	0.24	3.10	0.25	2.52	−0.44	3.44
10	−0.08	0.43	−0.28	0.49	−0.18	0.59	−0.42	0.68	−0.28	1.03

Note. Only a portion of this table is shown here to demonstrate its form and content. A machine-readable version is available for all 443 sources detected inside the PDR and outside the CO cores.

(This table is available in its entirety in machine-readable form in the online article.)

Table 21
The Sharpness and Chi Parameters for the Five HST Filters for Sources outside the PDR and Projected inside the CO Cores

	F275W Sharpness	F275W χ	F336W Sharpness	F336W χ	F438W Sharpness	F438W χ	F555W Sharpness	F555W χ	F625W Sharpness	F625W χ
1	0.11	0.70	0.05	0.83	0.14	1.41	0.77	4.14	−0.02	1.15
2	0.19	0.41	0.24	0.34	0.41	0.62	0.24	1.16	−0.13	0.63

Table 22
The Sharpness and Chi Parameters for the Five HST Filters for Sources outside the PDR and outside the CO Cores

	F275W Sharpness	F275W χ	F336W Sharpness	F336W χ	F438W Sharpness	F438W χ	F555W Sharpness	F555W χ	F625W Sharpness	F625W χ
1	−0.07	0.25	−0.22	0.31	0.02	0.32	0.01	0.49	−0.17	0.63
2	−0.11	0.32	−0.01	0.33	−0.11	0.50	−0.02	0.52	−0.43	1.62
3	0.08	0.11	−0.05	0.22	−0.01	0.40	0.05	0.51	−0.49	0.96
4	0.09	0.13	−0.11	0.34	0.57	2.00	0.65	2.02	−0.56	2.19
5	−0.05	0.26	−0.21	0.42	−0.01	0.46	−0.03	0.57	−0.14	0.65
6	0.01	0.26	−0.01	0.58	0.28	1.03	−0.11	0.63	−0.38	1.44
7	−0.62	0.17	−0.21	0.27	0.05	0.51	−0.04	0.85	−0.38	1.15
8	−0.25	0.20	−0.18	0.44	−0.10	1.51	−0.06	1.72	−0.38	2.86
9	−0.12	0.93	−0.06	0.92	0.10	1.34	0.16	1.08	−0.06	1.15
10	−0.05	0.17	−0.02	0.29	0.14	0.86	0.14	0.71	−0.22	1.24

Note. Only a portion of this table is shown here to demonstrate its form and content. A machine-readable version is available for all 566 sources detected outside the PDR and outside the CO cores.

(This table is available in its entirety in machine-readable form in the online article.)

Table 23
The Sharpness and Chi Parameters for the Four HST Filters for the Source inside the PDR and Projected inside the CO Cores Not Detected in the F275W Filter

	F336W Sharpness	F336W χ	F438W Sharpness	F438W χ	F555W Sharpness	F555W χ	F625W Sharpness	F625W χ
1	−0.23	0.27	0.04	0.24	0.46	0.60	−0.24	0.61

Table 24
The Sharpness and Chi Parameters for the Four HST Filters for Sources inside the PDR and outside the CO Cores Not Detected in the F275W Filter

	F336W Sharpness	F336W χ	F438W Sharpness	F438W χ	F555W Sharpness	F555W χ	F625W Sharpness	F625W χ
1	−0.05	0.22	−0.00	0.40	0.05	0.51	−0.49	0.95
2	−0.11	0.34	0.57	2.00	0.65	2.02	−0.56	2.19
3	−0.16	0.49	−0.14	0.61	−0.27	0.85	−0.28	0.98
4	−0.06	0.92	0.10	1.34	0.16	1.07	−0.06	1.15
5	−0.19	2.60	0.28	2.31	0.14	2.12	−0.51	3.68
6	0.03	0.35	0.04	0.47	0.10	0.80	−0.16	0.83
7	−0.29	0.21	0.10	0.53	0.13	0.53	−0.56	1.57
8	−0.18	0.34	0.07	0.94	0.05	0.96	−0.42	1.37
9	−0.38	0.29	−0.03	0.49	−0.02	0.54	−0.31	1.28
10	−0.13	0.20	−0.14	0.55	−0.05	1.23	−0.62	3.40

Note. Only a portion of this table is shown here to demonstrate its form and content. A machine-readable version is available for all 144 sources detected inside the PDR and outside the CO cores.

(This table is available in its entirety in machine-readable form in the online article.)

Table 25
The Sharpness and Chi Parameters for the Four HST Filters for Sources outside the PDR and outside the CO Cores Not Detected in the F275W Filter

	F336W Sharpness	F336W χ	F438W Sharpness	F438W χ	F555W Sharpness	F555W χ	F625W Sharpness	F625W χ
1	0.16	0.20	−0.01	0.63	0.05	1.00	−0.44	2.84
2	−0.30	0.30	−0.10	0.51	0.09	0.77	−0.28	1.88
3	−0.10	0.30	−0.05	1.27	−0.13	1.76	−0.21	4.00
4	−0.03	0.38	0.09	0.72	−0.04	1.25	−0.35	3.83
5	−0.13	0.29	0.28	0.90	0.17	1.08	−0.37	1.32
6	−0.37	0.28	−0.20	0.40	−0.10	0.50	−0.13	0.93
7	−0.07	0.21	−0.05	0.63	0.07	0.68	−0.13	1.55
8	−0.05	0.49	0.29	3.19	0.05	4.45	−0.23	5.18
9	−0.09	0.23	−0.02	0.55	0.06	0.68	−0.13	2.05
10	0.17	0.18	−0.13	0.78	0.05	1.35	−0.09	3.05

Note. Only a portion of this table is shown here to demonstrate its form and content. A machine-readable version is available for all 78 sources detected outside the PDR and outside the CO cores.

(This table is available in its entirety in machine-readable form in the online article.)

Appendix B
Spectral Energy Distribution Fits

Corner plots of the SED fits for a representative star from each of the seven categories based on their proximity to the PDR and CO cores, along with whether or not they were detected in the F275W filter, are show in Figures 10, 11, 12, 13, 14, 15, and 16. No additional stars were detected away from the PDR and projected inside the CO cores when excluding the F275W filter. The values shown in the plots are the posterior median (50th percentile) along with the 84th and 16th percentiles as the upper and lower errors, respectively, for each parameter. Figure 15 in particular shows how degeneracies between mass and age can result in multiple solutions.

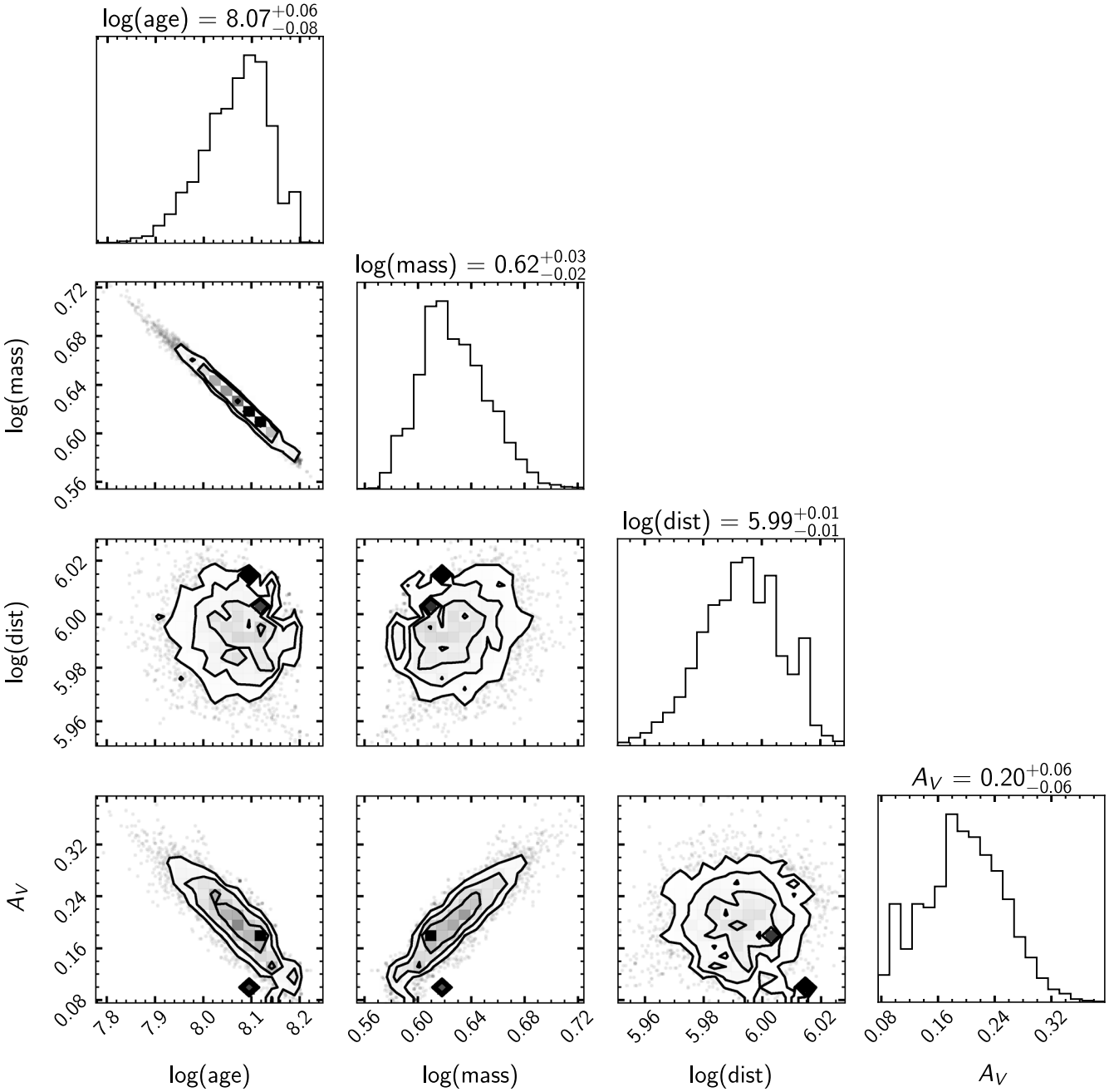

Figure 10. Corner plot of samples drawn from the posterior distribution for Star 1 in Table 11 of stars inside the PDR and projected inside the CO cores demonstrating the degeneracies between mass, age, distance, and dust.

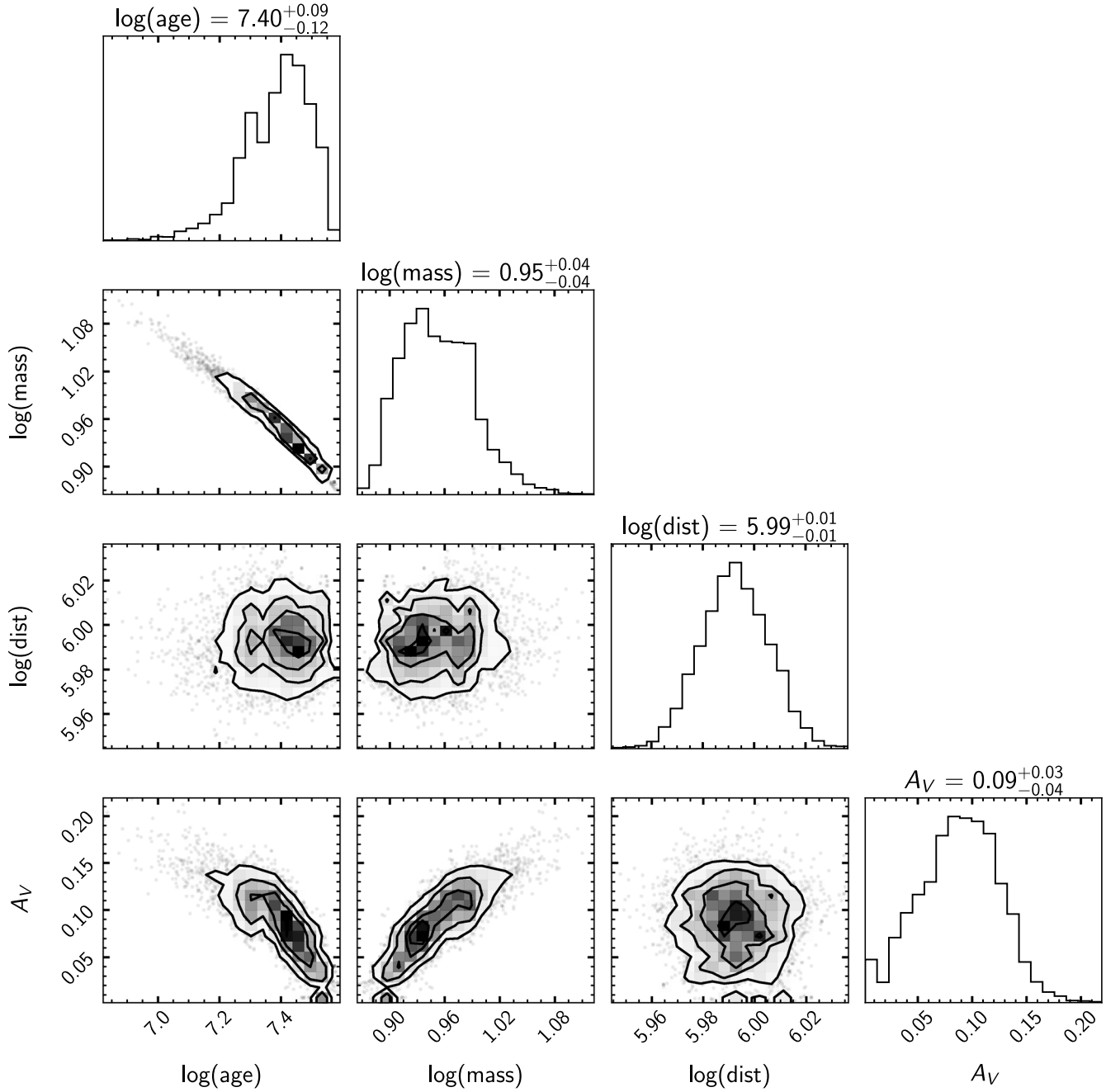

Figure 11. Corner plot of samples drawn from the posterior distribution for Star 3 in Table 12 of stars inside the PDR and away from the CO cores demonstrating the degeneracies between mass, age, distance, and dust.

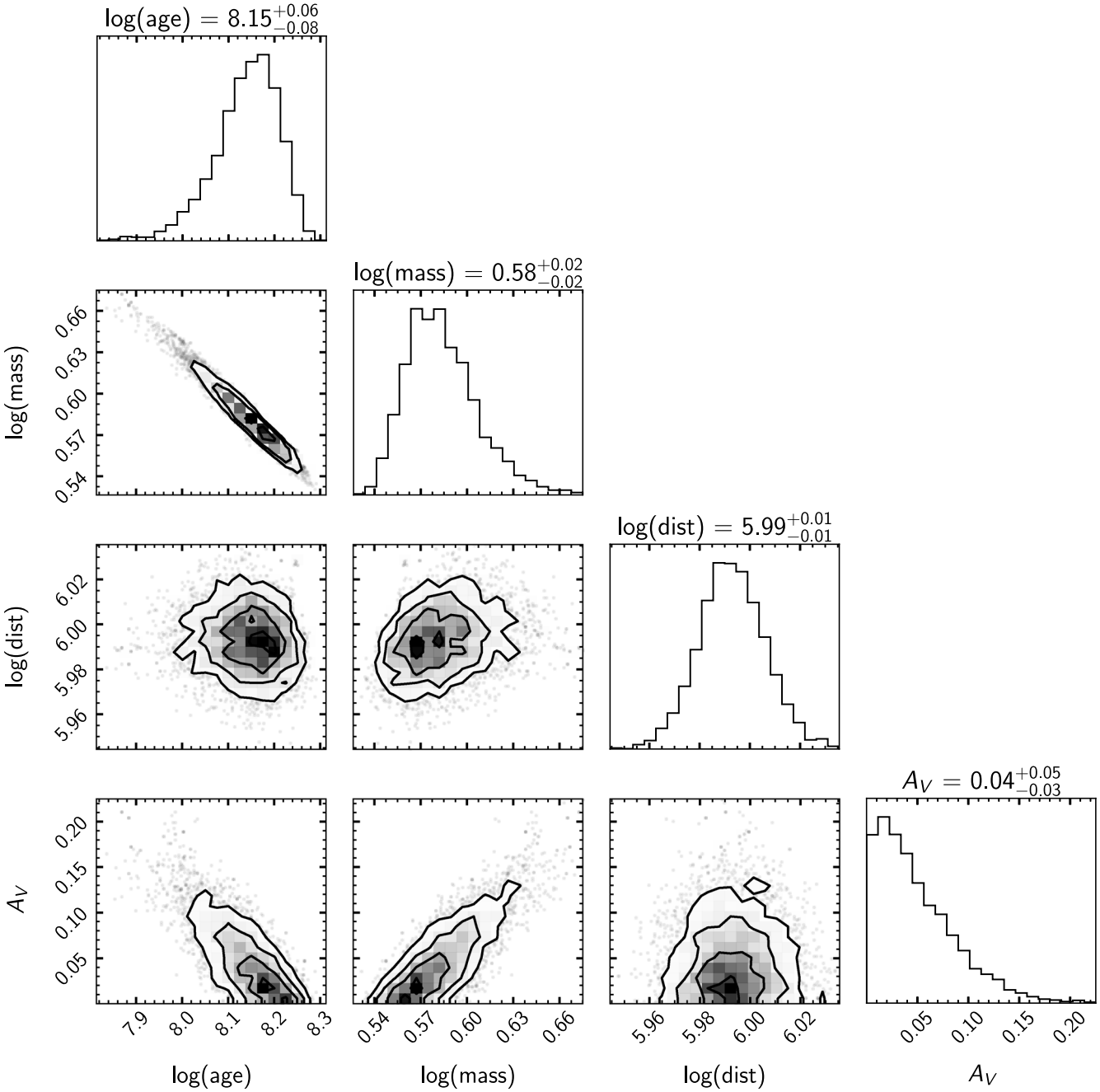

Figure 12. Corner plot of samples drawn from the posterior distribution for Star 2 in Table 13 of stars away from the PDR and projected inside the CO cores demonstrating the degeneracies between mass, age, distance, and dust.

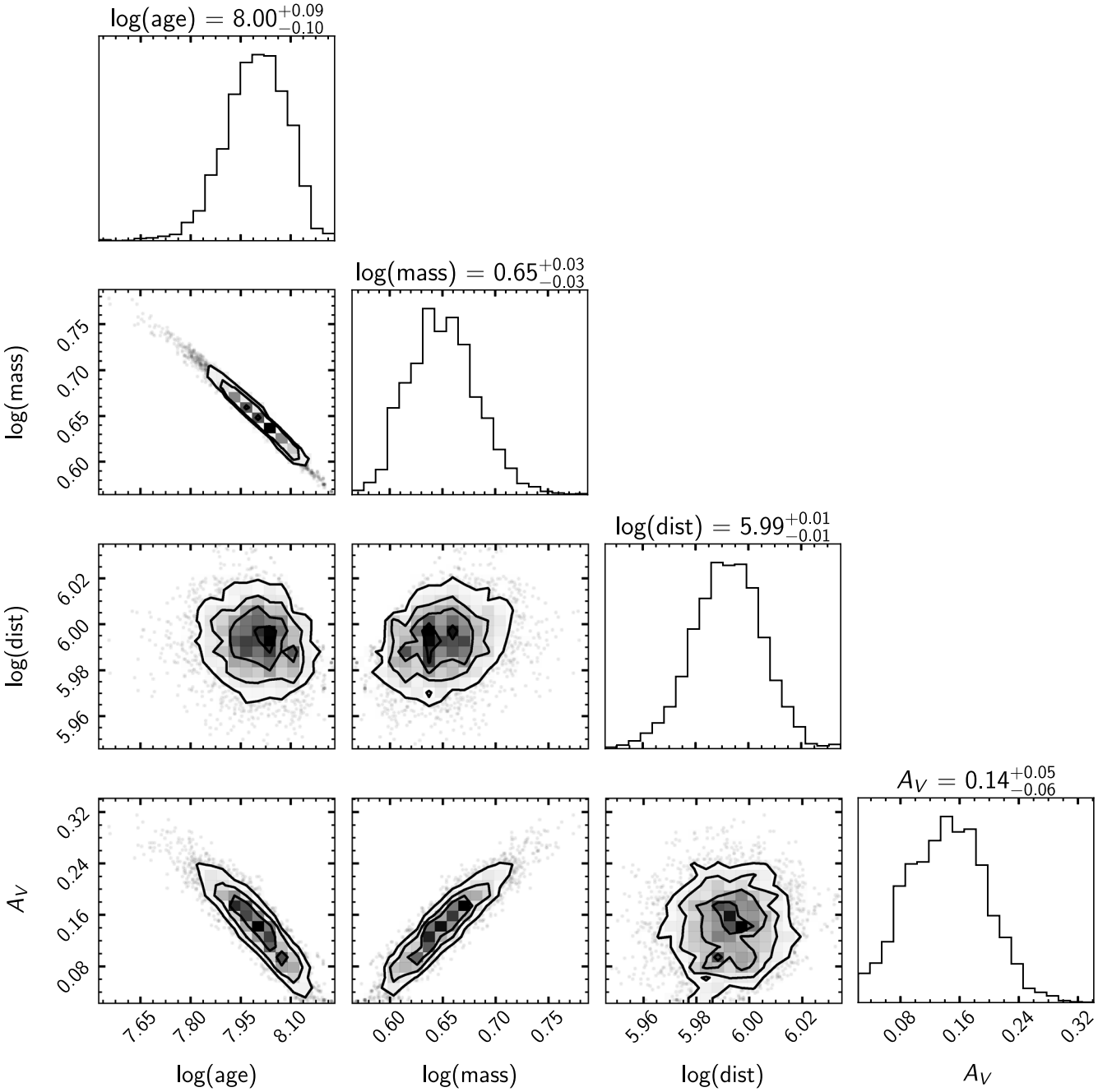

Figure 13. Corner plot of samples drawn from the posterior distribution for Star 5 in Table 14 of stars away from the PDR and away from the CO cores demonstrating the degeneracies between mass, age, distance, and dust.

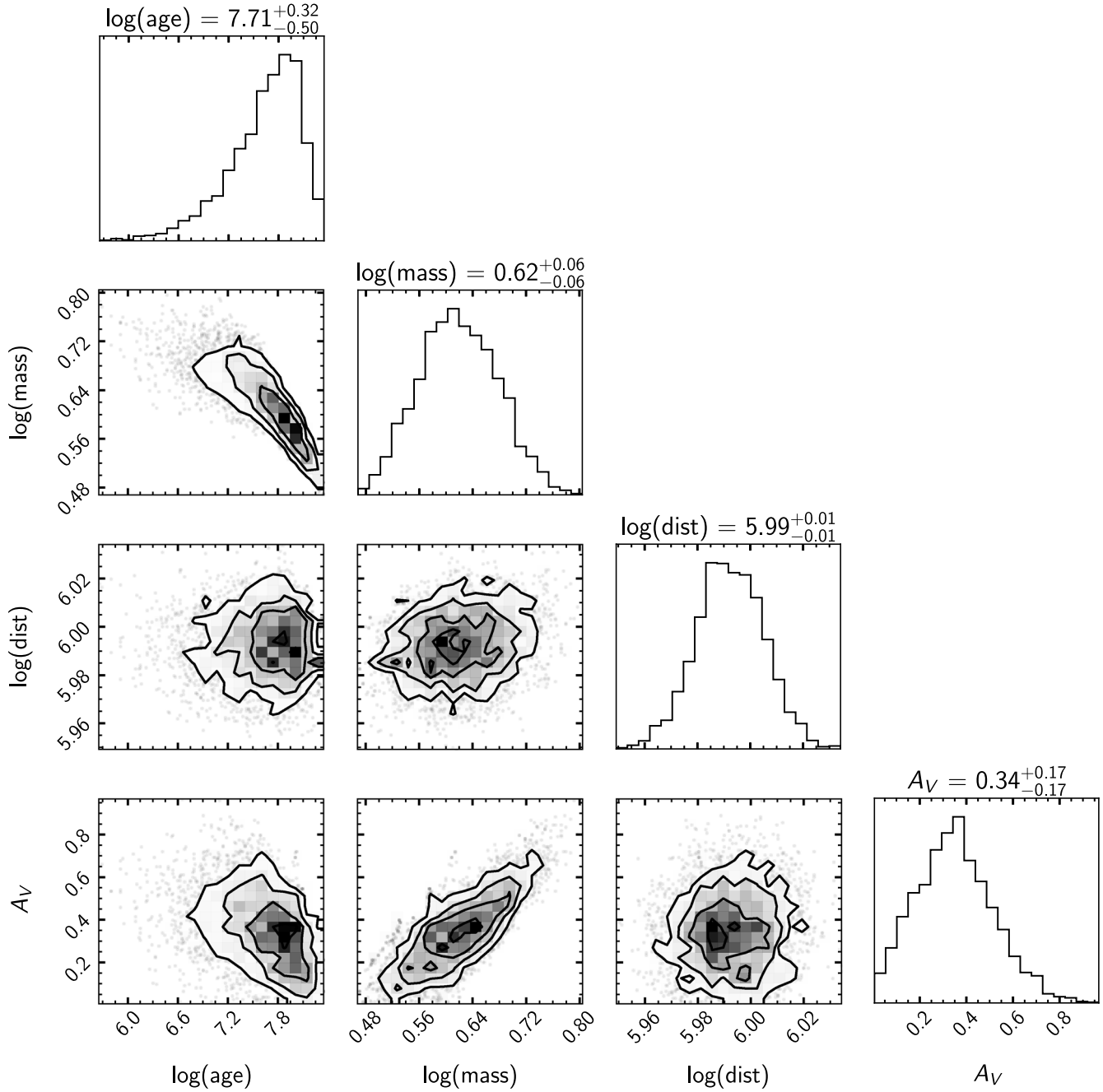

Figure 14. Corner plot of samples drawn from the posterior distribution for Star 1 in Table 15 of the star in the PDR and projected inside the CO cores not detected in the F275W filter demonstrating the degeneracies between mass, age, distance, and dust.

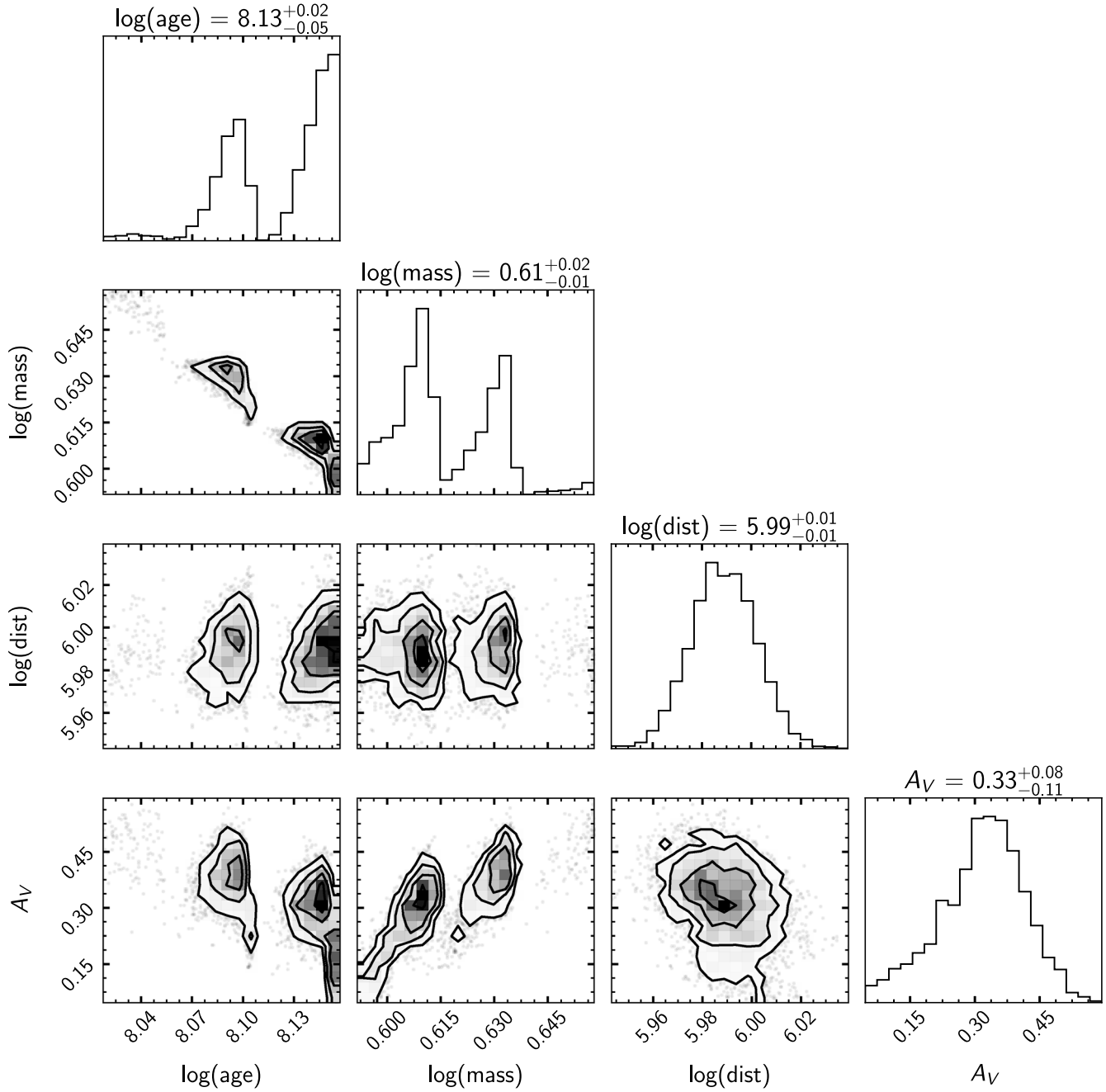

Figure 15. Corner plot of samples drawn from the posterior distribution for Star 1 in Table 16 of stars in the PDR and away from the CO cores not detected in the F275W filter demonstrating the degeneracies between mass, age, distance, and dust.

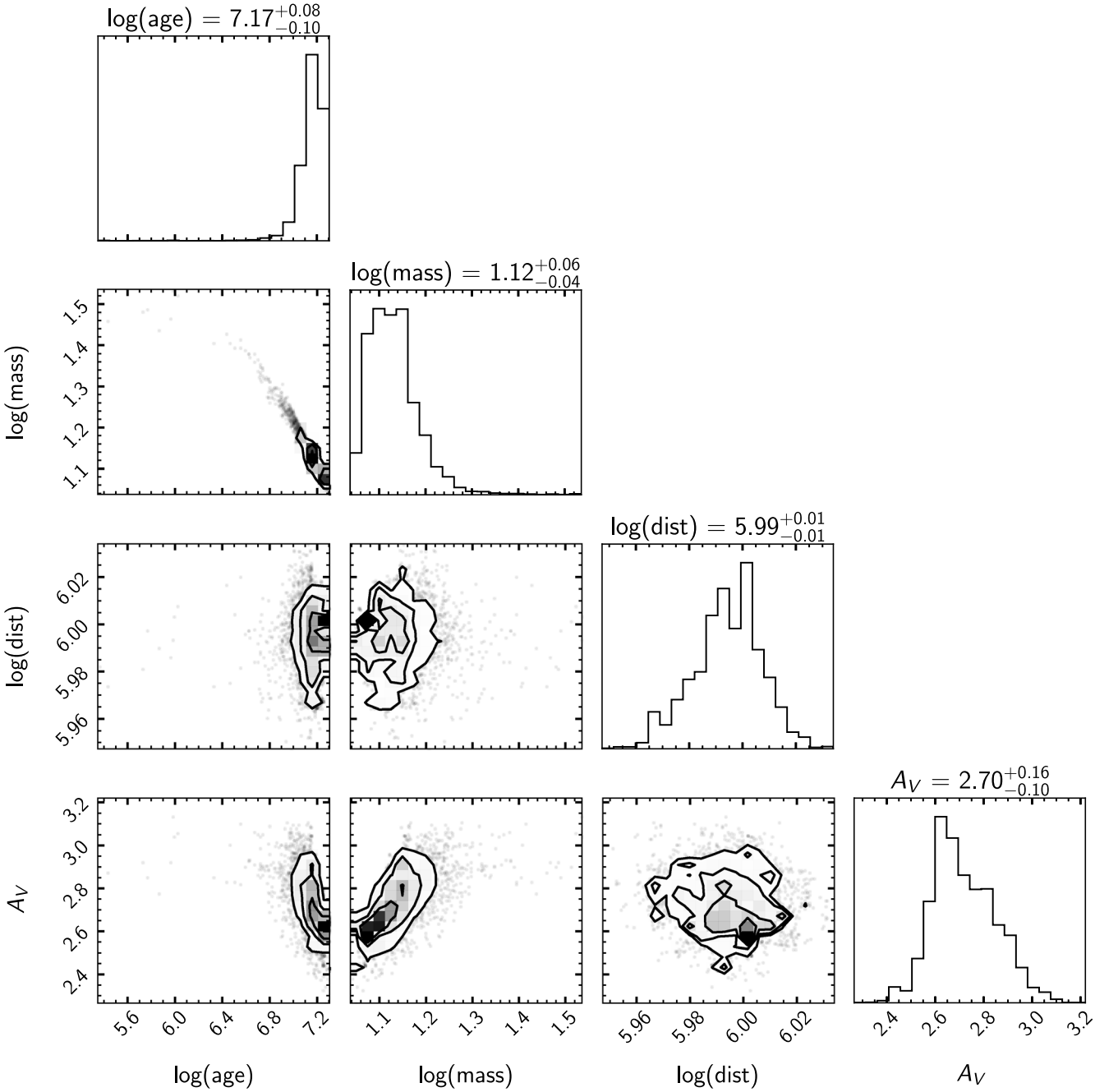

Figure 16. Corner plot of samples drawn from the posterior distribution for Star 6 in Table 17 of stars away from the PDR and away from the CO cores not detected in the F275W filter demonstrating the degeneracies between mass, age, distance, and dust.

ORCID iDs

Haylee N. Archer https://orcid.org/0000-0002-8449-4815
Deidre A. Hunter https://orcid.org/0000-0002-3322-9798
Bruce G. Elmegreen https://orcid.org/0000-0002-1723-6330
Leslie K. Hunt https://orcid.org/0000-0001-9162-2371
Rosalia O'Brien https://orcid.org/0000-0003-3351-0878
Elias Brinks https://orcid.org/0000-0002-7758-9699
Phil Cigan https://orcid.org/0000-0002-8736-2463
Monica Rubio https://orcid.org/0000-0002-5307-5941
Rogier A. Windhorst https://orcid.org/0000-0001-8156-6281
Rolf A. Jansen https://orcid.org/0000-0003-1268-5230
Elijah P. Mathews https://orcid.org/0000-0003-0384-0681

References

Albers, S. M., Weisz, D. R., Cole, A. A., et al. 2019, MNRAS, 490, 5538
Anderson, J., Baggett, S., & Kuhn, B. 2021, Updating the WFC3/UVIS CTE Model and Mitigation Strategies Instrument Science Report 2021-9, STScI
Annunziatella, M., Mercurio, A., Brescia, M., Cavuoti, S., & Longo, G. 2013, PASP, 125, 68
Archer, H. N., Cigan, P., Elmegreen, B., et al. 2022a, Young Stars and Gas Structure within the ALMA Coverage of Dwarf Irregular Galaxy WLM Cycle 30, ID. #17068, HST Proposal
Archer, H. N., Hunter, D. A., Elmegreen, B. G., et al. 2022b, AJ, 163, 141
Bezanson, J., Edelman, A., Karpinski, S., & Shah, V. B. 2017, SIAMR, 59, 65
Bolatto, A. D., Wolfire, M., & Leroy, A. K. 2013, ARA&A, 51, 207
Boyer, M. L., Pastorelli, G., Girardi, L., et al. 2024, ApJ, 973, 120
Bressan, A., Marigo, P., Girardi, L., et al. 2012, MNRAS, 427, 127

Brosch, N., Heller, A., & Almoznino, E. 1998, ApJ, 504, 720
Chen, Y., Bressan, A., Girardi, L., et al. 2015, MNRAS, 452, 1068
Chen, Y., Girardi, L., Bressan, A., et al. 2014, MNRAS, 444, 2525
Chevance, M., Kruijssen, J. M. D., Hygate, A., et al. 2020a, MNRAS, 493, 2872
Chevance, M., Madden, S. C., Fischer, C., et al. 2020b, MNRAS, 494, 5279
Choi, J., Dotter, A., Conroy, C., et al. 2016, ApJ, 823, 102
Cigan, P., Young, L., Cormier, D., et al. 2016, AJ, 151, 14
Cormier, D., Bendo, G. J., Hony, S., et al. 2017, MNRAS, 468, L87
Dale, D. A., Cohen, S. A., Johnson, L. C., et al. 2009, ApJ, 703, 517
Draine, B. T., & Li, A. 2007, ApJ, 657, 810
Elmegreen, B. G. 1989, ApJ, 338, 178
Elmegreen, B. G. 2000, ApJ, 530, 277
Elmegreen, B. G., Morris, M., & Elmegreen, D. M. 1980, ApJ, 240, 455
Elmegreen, B. G., Rubio, M., Hunter, D. A., et al. 2013, Natur, 495, 487
Fukui, Y., & Kawamura, A. 2010, AARA, 48, 547
Gordon, K. D., Clayton, G. C., Misselt, K. A., Landolt, A. U., & Wolff, M. J. 2003, ApJ, 594, 279
Gordon, K. D., Fouesneau, M., Arab, H., et al. 2016, ApJ, 826, 104
Harris, C. R., Millman, K. J., van der Walt, S. J., et al. 2020, Natur, 585, 357
Hoffman, M. D., & Gelman, A. 2011, arXiv:1111.4246
Hoffmann, S. L., Mack, J., Avila, R., et al. 2021, AAS Meeting Abstracts, 53, 216.02
Hu, C.-Y., Schruba, A., Sternberg, A., & van Dishoeck, E. F. 2022, ApJ, 931, 28
Hu, C.-Y., Sternberg, A., & van Dishoeck, E. F. 2021, ApJ, 920, 44
Hu, C.-Y., Sternberg, A., & van Dishoeck, E. F. 2023, ApJ, 952, 140
Hunt, L. K., Belfiore, F., Lelli, F., et al. 2023, A&A, 675, A64
Hunter, D. A., Elmegreen, B. G., & Madden, S. C. 2024, ARA&A, 62, 113
Hunter, D. A., Wilcots, E. M., van Woerden, H., Gallagher, J. S., & Kohle, S. 1998, ApJL, 495, L47
Hunter, D. A., Ficut-Vicas, D., Ashley, T., et al. 2012, AJ, 144, 134
Hunter, J. D. 2007, CSE, 9, 90
Iorio, G., Fraternali, F., Nipoti, C., et al. 2017, MNRAS, 466, 4159
Kingma, D. P., & Ba, J. 2017, arXiv:1412.6980
Kroupa, P. 2002, Sci, 295, 82
Krumholz, M. R., Dekel, A., & McKee, C. F. 2012, ApJ, 745, 69
Leaman, R., Venn, K. A., Brooks, A. M., et al. 2012, ApJ, 750, 33
Lee, A. J., Freedman, W. L., Madore, B. F., et al. 2021, ApJ, 907, 112
Lee, H., Skillman, E. D., & Venn, K. A. 2005, ApJ, 620, 223
Leja, J., Johnson, B. D., Conroy, C., et al. 2019, ApJ, 877, 140
Leroy, A. K., Walter, F., Brinks, E., et al. 2008, AJ, 136, 2782
Madden, S. C. 2022, EPJWC, 265, 00011
Madden, S. C., Cormier, D., Hony, S., et al. 2020, A&A, 643, A141
Marigo, P., Girardi, L., Bressan, A., et al. 2017, ApJ, 835, 77
Martin, D. C., Fanson, J., Schiminovich, D., et al. 2005, ApJL, 619, L1
McQuinn, K. B. W., B. Newman, M. J., Savino, A., et al. 2024, ApJ, 961, 16
Mogensen, P. K., & Riseth, A. N. 2018, JOSS, 3, 615
Newman, M. J. B., McQuinn, K. B. W., Skillman, E. D., et al. 2024, ApJ, 975, 195
Nicolet, B. 1980, A&AS, 42, 283
Osman, O., Bekki, K., & Cortese, L. 2020, MNRAS, 497, 2002
Pastorelli, G., Marigo, P., Girardi, L., et al. 2019, MNRAS, 485, 5666
Pastorelli, G., Marigo, P., Girardi, L., et al. 2020, MNRAS, 498, 3283
Pedregosa, F., Varoquaux, G., Gramfort, A., et al. 2011, JMLR, 12, 2825
Peltonen, J., Rosolowsky, E., Williams, T. G., et al. 2024, MNRAS, 527, 10668
Pineda, J. L., Langer, W. D., & Goldsmith, P. F. 2014, A&A, 570, A121
Planck Collaboration, Ade, P. A. R., Aghanim, N., et al. 2011, A&A, 536, A19
Ramambason, L., Lebouteiller, V., Madden, S. C., et al. 2024, A&A, 681, A14
Requena-Torres, M. A., Israel, F. P., Okada, Y., et al. 2016, A&A, 589, A28
Rubio, M., Elmegreen, B. G., Hunter, D. A., et al. 2015, Natur, 525, 218
Saldaño, H. P., Rubio, M., Bolatto, A. D., et al. 2023, A&A, 672, A153
Stan Development Team 2025, RStan: the R Interface to Stan, https://mc-stan.org/
Stetson, P. B. 1987, PASP, 99, 191
Tang, J., Bressan, A., Rosenfield, P., et al. 2014, MNRAS, 445, 4287
Taylor, C. L., Kobulnicky, H. A., & Skillman, E. D. 1998, AJ, 116, 2746
Teyssier, M., Johnston, K. V., & Kuhlen, M. 2012, MNRAS, 426, 1808
Tody, D. 1986, Proc. SPIE, 627, 733
Wakelam, V., Bron, E., Cazaux, S., et al. 2017, MolAs, 9, 1
Wang, Y., Gao, J., Ren, Y., & Chen, B. 2022, ApJS, 260, 41
Weisz, D. R., McQuinn, K. B. W., Savino, A., et al. 2023, ApJS, 268, 15
Windhorst, R. A., Cohen, S. H., Hathi, N. P., et al. 2011, ApJS, 193, 27
Windhorst, R. A., Carleton, T., O'Brien, R., et al. 2022, AJ, 164, 141
Wolfire, M. G., Hollenbach, D., & McKee, C. F. 2010, ApJ, 716, 1191
Xu, K., Ge, H., Tebbutt, W., et al. 2020, PMLR, 118, 10
Zhang, H.-X., Hunter, D. A., Elmegreen, B. G., Gao, Y., & Schruba, A. 2012, AJ, 143, 47